GEOLOGICA CARPATHICA, APRIL 2022, 73, 2, 97–122 https://doi.org/10.31577/GeolCarp.73.2.1

Variscan metamorphism and partial melting of sillimanite-bearing metapelites in the High Tatra Mts. constrained by Th–U–Pb dating of monazite

MARIAN JANÁK[1,✉], IGOR PETRÍK[1], PATRIK KONEČNÝ[2], SERGII KURYLO[3], MILAN KOHÚT[1] and JÁN MADARÁS[1]

[1]Earth Science Institute, Slovak Academy of Sciences, Dúbravská cesta 9, P.O. Box 106, 840 05 Bratislava, Slovakia; ✉marian.janak@savba.sk
[2]Dionýz Štúr State Geological Institute, Mlynská dolina 1, 817 04 Bratislava, Slovakia
[3]Earth Science Institute, Slovak Academy of Sciences, Ďumbierska 1, 974 11 Banská Bystrica, Slovakia

(Manuscript received December 3, 2021; accepted in revised form February 8, 2022; Associate Editor: Igor Broska)

Abstract: The Tatra Mountains of the Western Carpathians are a key area for the study of the eastern continuation of the Variscan basement within the Alpine–Carpathian orogenic belt in Central Europe. Metamorphic zonation in the Tatra Mts. displays an inverted metamorphic sequence related to Variscan thrusting and emplacement of gneisses, migmatites and granites over micaschists. Here we present new results of Th–U–Pb dating of monazite in sillimanite-bearing metapelitic gneisses, migmatite and granodiorite from the High Tatra along with petrological interpretation based on thermodynamic modelling. The metapelitic gneisses show the peak metamorphic assemblage garnet+sillimanite+plagioclase+biotite+muscovite+ilmenite+quartz; inclusions of rutile, phengitic muscovite and paragonite in the garnet core indicate an earlier metamorphic stage. Thermodynamic modelling suggests a clockwise, prograde *P–T* path via staurolite-to-sillimanite sequence reactions from above 6 kbar to ca. 5–6 kbar and 650–700 °C, at mid-crustal levels. Migmatites, with dominant K-feldspar, plagioclase ($An_{12–35}$) and quartz in the leucosome, underwent partial melting involving biotite dehydration reactions and formation of peritectic, Mn-rich garnet and/or Ti-magnetite at ca. 7–8 kbar and 760–770 °C, during decompression from lower-crustal levels. Monazite composition in metapelitic gneisses differs from that in leucosome of migmatite. The latter shows pronounced Eu-negative anomalies interpreted as the result of co-crystallization with feldspars and higher Y contents indicating higher temperature of crystallization. Monazite ages are identical within 2σ errors and indicate that both metamorphic and melting events occurred in Early Carboniferous, between 350–345 Ma as a consequence of continental collision and crustal thickening in the course of the Variscan orogeny.

Keywords: Th–U–Pb dating of monazite, metapelites, partial melting, Variscan orogeny, Tatra Mts., Western Carpathians.

Introduction

This paper deals with high-grade metapelites from the Tatra Mountains in the Western Carpathians (Slovakia), a key area for the study of the eastern continuation of the Variscan basement within the Alpine–Carpathian orogenic belt in Central Europe (Fig. 1). Metamorphic zonation in the Tatra Mts. displays an inverted metamorphic sequence with high-grade rocks (gneiss, migmatite, amphibolite, eclogite) of kyanite and sillimanite zone in the hangingwall and lower-grade rocks (micaschist) of staurolite–kyanite and kyanite–fibrolite zone in the footwall (Fig. 2a), related to Variscan thrusting (Janák 1994; Janák et al. 1999). Most details on Variscan metamorphic evolution of the Tatra Mts. are known from the Western Tatra (e.g. Janák 1994; Janák et al. 1996, 1999; Poller et al. 2000; Moussallam et al. 2012; Burda et al. 2021). In the High Tatra, metamorphic rocks are less abundant and belong to the sillimanite zone (Fig. 2a). Age data on the High Tatra are known mostly from zircon dating of granitoids (Poller & Todt 2000; Poller et al. 2001; Burda et al. 2013a,b; Gawęda et al. 2016; Kohút & Larionov 2021; Broska et al. 2022). Most of the data record metamorphism and magmatism in Late Devonian and Carboniferous time (ca. 365–330 Ma).

Monazite is one of the most important accessory minerals in metapelitic lithologies, stable at various *P–T* conditions of metamorphism and partial melting (e.g. Zhu & O'Nions 1999; Terry et al. 2000; Catlos et al. 2002; Spear & Pyle 2002; Hermann & Rubatto 2003; Kohn et al. 2005; Janots et al. 2008; Krenn et al. 2009; Gieré et al. 2011; Majka et al. 2012; Engi 2017; Skrzypek et al. 2017; Hacker et al. 2019; Petrík et al. 2019). Monazite typically contains large amounts of radioactive elements and can be dated using various methods (isotope dilution, LA-ICPMS, ion microprobe, electron microprobe). Electron microprobe chemical dating method (Parrish 1990; Suzuki & Adachi 1991; Montel et al. 1996; Finger et al. 1998; Cocherie & Albarede 2001; Suzuki & Kato 2008; Konečný et al. 2018) produces typically an error of 5–8 % (2 σ) for individual dates (caused mostly by analytical error of Pb determination) and 1.5–2 % for weighted averages and isochrons, which is sufficient for the distinction of main magmatic and metamorphic events. U–Th–Pb chemical dating of monazite was also applied to granitic and metamorphic rocks in the Western Carpathians (e.g. Finger et al. 2003; Petrík & Konečný 2009; Broska & Petrík 2015; Petrík et al. 2020). The composition of metamorphic monazite commonly occurring in metapelites and migmatites, either in the matrix or

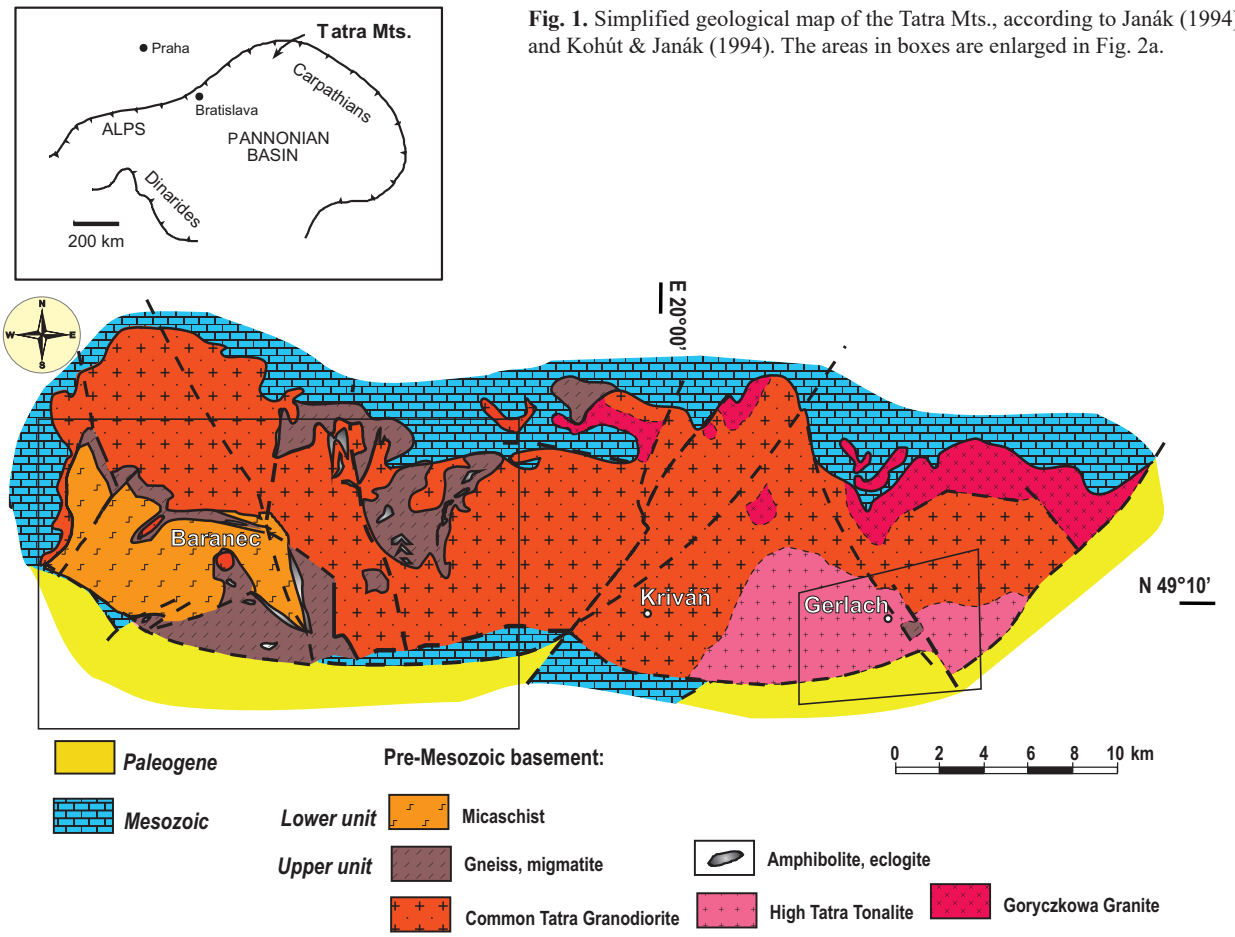

Fig. 1. Simplified geological map of the Tatra Mts., according to Janák (1994) and Kohút & Janák (1994). The areas in boxes are enlarged in Fig. 2a.

within garnet, provides additional information to the age determination, especially by its Y contents or Eu anomalies. The first is proportional to temperature – if the rock is saturated by Y, it can be used as a monazite–xenotime thermometer (Heinrich et al. 1997; Pyle et al. 2001; Seydoux-Guillaume et al. 2002). The second may indicate redox regime or, in melt-bearing rocks, fractionation of plagioclase.

Partial melting is a fundamental mechanism for differentiating continental crust. Fluid-absent partial melting of biotite-bearing metapelites represents an important process for generating granitic melts (e.g. Clemens & Vielzeuf 1987; Le Breton & Thompson 1988). Partial melting is observed in migmatised metapelites of the Tatra Mountains. Textural, thermobarometric, fluid-inclusion and age data indicate that these rocks followed a clockwise *P–T* path, involving muscovite and biotite dehydration-melting reactions during decompression and exhumation of Variscan continental crust (Janák et al. 1999; Moussallam et al. 2012).

In this article, we present new results of Th–U–Pb dating of monazite in sillimanite-bearing metapelitic gneisses and migmatite from the High Tatra along with petrological interpretation based on thermodynamic modelling. The purpose of this paper is to determine: (1) *P–T* conditions of metamorphism and partial melting, (2) melting reactions involving biotite dehydration reactions, and (3) monazite composition and age data constraining timing of metamorphism and partial melting.

Geological setting

The Tatra Mountains are located in the northernmost sector of the Western Carpathians (Fig. 1). They are a representative of the so-called core mountains within the Tatric unit, a major tectonic unit of the Western Carpathians (Andrusov 1968; Plašienka et al. 1998; Plašienka 2018). The crystalline basement of the Tatra Mts. (Fig. 1) is composed of pre-Mesozoic metamorphic rocks and granites, overlain by Mesozoic and Cenozoic sedimentary cover sequences and nappes. Metamorphic rocks are abundant in the western part (Western Tatra), whereas in the eastern part (the High Tatra) they occur as minor bodies in granites (Figs. 1 and 2). Two superimposed tectonic units – lower and upper, differing in lithology and metamorphic grade, have been distinguished (Janák 1994; Janák et al. 1999). These units are separated by a Variscan thrust fault – a major tectonic discontinuity in the crystalline basement of the Tatra Mts. (Fig. 2).

The lower unit is exposed in the Western Tatra as a tectonic window of up to 1000-m thickness (Fig. 2); it is composed of micaschists. Metapelitic micaschists with garnet, kyanite,

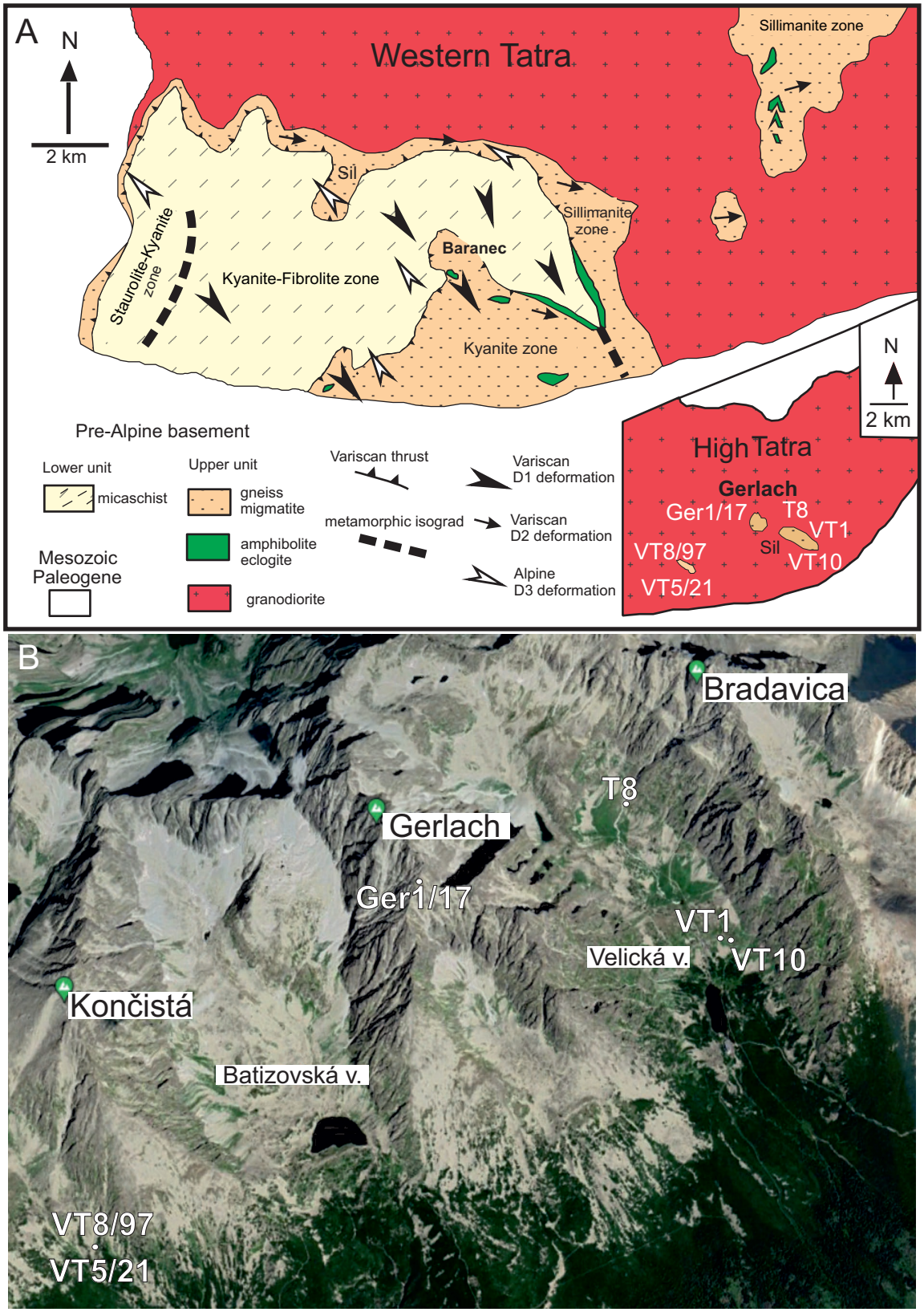

Fig. 2. A — Generalised tectono-metamorphic map of the Tatra Mountains according to Janák et al. (1999) with locations of investigated samples. **B** — Google map of the High Tatra with locations of investigated samples.

staurolite, and fibrolitic sillimanite alternate with quartz-rich metapsammites, resembling flysch sediments (Kahan 1969). Metamorphic *P–T* conditions reached 5–6 kbar/550–620 °C in the staurolite-kyanite zone and 6–8 kbar/620–660 °C in the kyanite–sillimanite (fibrolite) zone (Janák 1994). The upper unit is composed of para- and orthogneisses, amphibolites, migmatites, calc-silicates and granitoids. In the kyanite zone paragneisses contain kyanite partly transformed to sillimanite and orthogneisses show augen-like porphyroclasts of K-feldspar. Relics of eclogites (retrogressed eclogites) occur in amphibolites at the base of the upper unit (Baranec area) within the kyanite zone. These amphibolites are banded, with felsic layers of tonalitic to trondhjemitic composition. Metamorphism in the kyanite zone reached eclogite facies at P>15 kbar/700 °C followed by high-pressure granulite/high-pressure amphibolite facies overprint at ca. 10–14 kbar/700–750 °C (Janák et al. 1996). Paragneisses with prismatic sillimanite (sillimanite zone) and rarely cordierite occur at higher levels of the upper unit. They show migmatisation and partial melting due to dehydration reactions of muscovite and biotite at 6–10 kbar/700–800 °C (Janák et al. 1999). Calc silicate rocks occur only sporadically in the sillimanite zone of the High Tatra. These rocks contain andradite–grossular garnet, diopside–hedenbergite clinopyroxene, epidote–clinozoisite, carbonate (calcite) and quartz (Pawlica 1918; Janák 1993). According to Janák (1993), calc-silicate rocks are metacarbonates with minor pelitic component, metamorphic *P–T* conditions reached ca. 5 kbar and 650 °C. Sillimanite zone gneisses and migmatites are intruded by a sheet-like granitoid pluton (Gorek 1959). Granitoids range from leucogranite to biotite tonalite and amphibole diorite (Kohút & Janák 1994).

Polyphase Variscan and Alpine deformation under distinct *P–T* conditions and kinematics (Fig. 2) has been recognised (Fritz et al. 1992; Janák et al. 1999). Variscan deformation (D_1) under ductile conditions is demonstrated by kinematic indicators suggesting top-to-the-south, southeast thrusting and emplacement of the upper unit onto the lower one. Variscan deformation (D_2) is generally dextral, or top-to-the-east, related to orogen-parallel extension. Alpine deformation (D_3) under brittle conditions is manifested by top-to-the-northwest shear, which is attributed to a Late Cretaceous contractional event.

Investigated samples

The investigated samples are metapelitic gneiss (Ger1/17, VT1, VT10), migmatite (VT8/97, VT5/21) and granodiorite (T8). Metapelitic gneiss and migmatite come from the sillimanite zone in the High Tatra and have been collected from the following localities (Fig. 2): Gerlach peak (Ger1/17), Velická valley (VT1, VT10) and Končistá peak. Near the peak of Mt. Gerlach, which is the highest peak of the Tatra Mts. (altitude 2655 m), metapelitic gneiss crops out together with calc-silicate rock (altitude 2500–2550 m), forming layers of 2–15 meters thickness in granodiorite (Fig. 3). In Velická valley, the metapelitic gneiss crops out as a band (several tens of meters thick) in the walls of granodiorite (Fig. 4). The investigated migmatite (VT8/97, VT5/97) comes from a small outcrop (ca. 20 m) along a footpath below the southern ridge of Končistá peak (Fig. 5). Generally, all outcrops show metamorphic foliation dipping 40–60° N, NW with lineation and b-axis of folds in N–S and NW–SE direction. Granodiorite (T8) comes from the upper part of Velická valley (Fig. 2).

Analytical methods

Electron microprobe WDS analysis of mineral chemistry was performed with a JEOL JXA 8530F instrument in the Earth Science Institute, Slovak Academy of Sciences in Banská Bystrica. The operating conditions were as follows: 15 kV accelerating voltage, 20 nA beam current, counting times 10–20 s on peaks and beam diameter of 2–7 μm depending at grain size. Ti-magnetite (ulvöspinel) and ilmenohematite phases were analysed by a beam defocused to 10 μm in order to include finer exsolutions. Mineral standards (Si: albite, diopside, Ca, Mg: diopside, Na: albite, K: orthoclase, Mn: rhodonite, Fe: hematite, Zn: gahnite, Ba, S: barite, P: apatite, Sr: celestite, Ti: rutile, F: fluorite, Cl: tugtupite), pure element oxides (Cr: Cr_2O_3, Sc: $ScVO_4$) were used for calibration. Calculation of concentration was provided by ZAF correction method.

Micro-Raman spectroscopy was used to identify sillimanite and other micro-inclusions with two confocal instruments: (1) Thermo-Scientific DXR Raman Microscope at the Institute of Chemistry, Slovak Academy of Sciences, Bratislava (2) LabRAM-HR 800 (Horiba Jobin-Yvon) at the Earth Science Institute of the Slovak Academy of Sciences in Banská Bystrica.

Mineral abbreviations are according to Whitney & Evans (2010).

Results

Petrography and mineral chemistry

Metapelitic gneisses

The rock texture is medium-grained, the foliation is defined by preferred orientation of biotite and quartz-feldsphatic portions forming felsic layers and segregations (Figs. 3, 4). The rocks contain garnet, sillimanite, biotite, muscovite, quartz and plagioclase as major mineral phases. Rutile and ilmenite represent Fe–Ti oxides, rutile has been often partially replaced by ilmenite. Staurolite is rarely present as inclusions in garnet. Other minor and accessory minerals include tourmaline, apatite, zircon and monazite. Prismatic sillimanite and biotite (Fig. 6a) are mostly oriented parallel to foliation whereas muscovite often crosscuts the foliation. Felsic layers

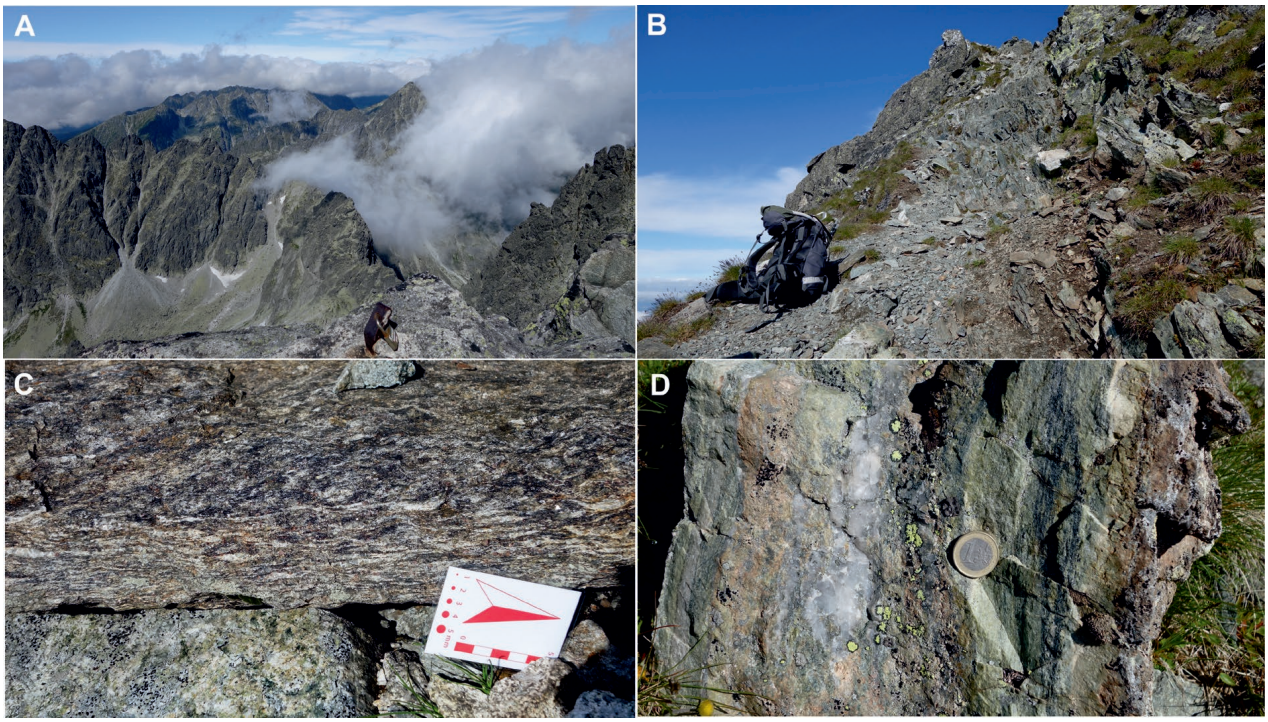

Fig. 3. Metapelitic gneiss and calc-silicate from Gerlach peak. **A** — View from the summit of Gerlach peak. **B** — Outcrop of gneiss and calc-silicate rocks in granodiorite (altitude 2510 m). **C** — Metapelitic gneiss texture with biotite, garnet, plagioclase and quartz. **D** — Calc-silicate texture with garnet (reddish), clinopyroxene, epidote (light-green), amphibole (dark-green) and quartz.

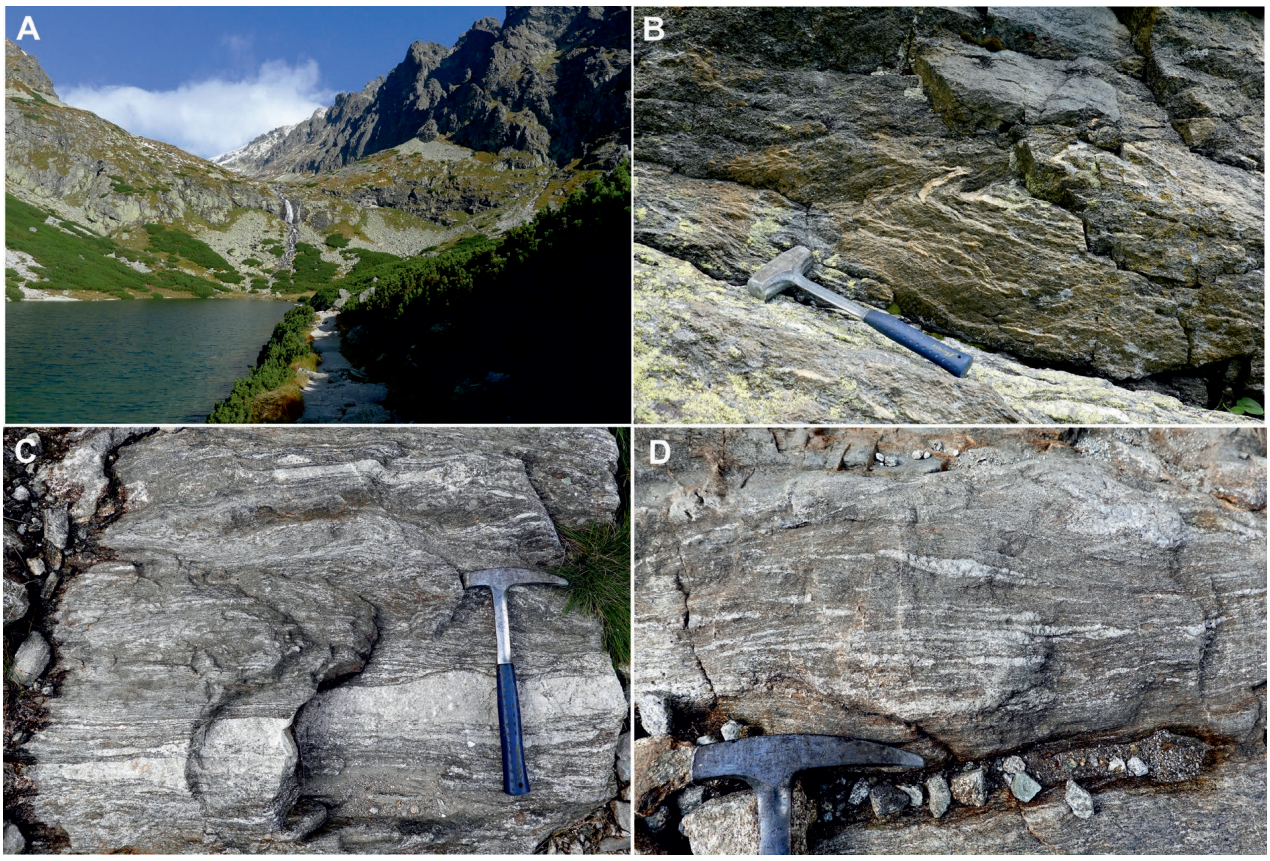

Fig. 4. Metapelitic gneiss and migmatite from the Velická valley. **A** — Large outcrop in the valley above the lake to the right of waterfall ("Večný dážď"). **B** — Metapelitic gneiss showing folding of metamorphic foliation. **C**, **D** — Inhomogeneous texture of gneiss to migmatite with biotite-rich melanocratic and quartz–feldshpar leucocratic layers and segregations.

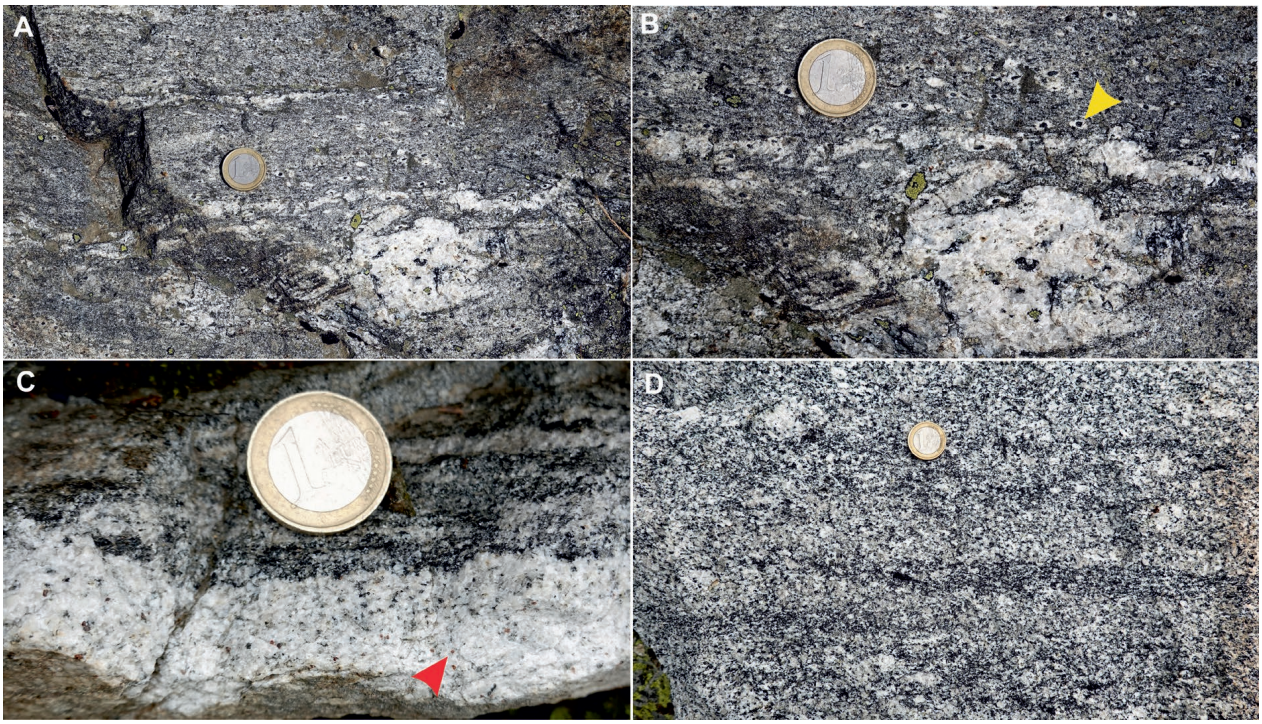

Fig. 5. Diatexite and granodiorite from Končistá. **A**, **B** — Diatexite texture with quartz-feldspar leucosome segregations and magnetite (marked by arrow). **C** — Leucosome with small euhedral garnets (marked by arrow). **D** — Granodiorite (High Tatra type).

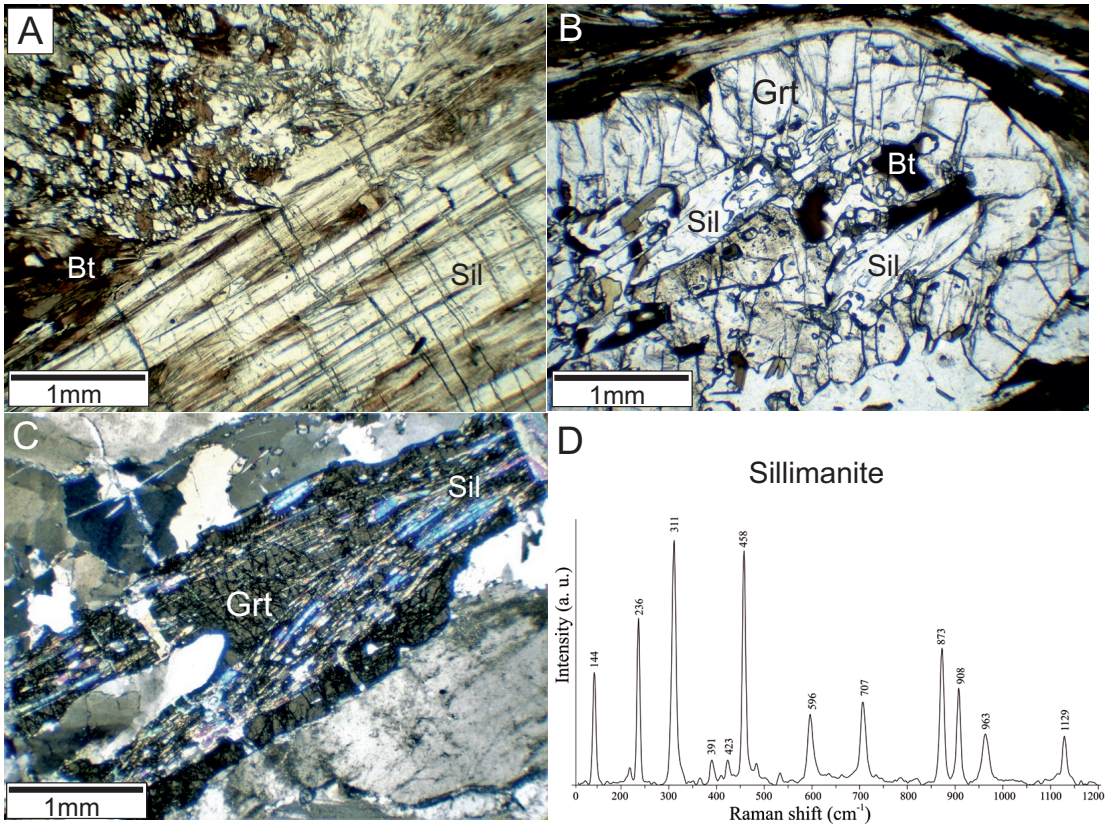

Fig. 6. A–**C** — Photomicrgraphs of sillimanite and garnet in metapelitic gneisses from the Velická valley. **A** — Prismatic sillimanite and biotite in the matrix. **B** — Prismatic sillimanite and biotite inclusions in garnet. Sample VT10. **C** — Garnet of elongate shape with needles of sillimanite. The garnet shows fractures and dislocations, quartz grains show a lobate morphology and chessboard extinction. **D** —Raman spectrum of sillimanite.

are composed of plagioclase and quartz, K-feldspar was not observed in the investigated gneisses. Garnet encloses prismatic sillimanite and biotite (Fig. 6b), these inclusions are often oriented oblique to the external foliation and may preserve an earlier fabric. Some of these garnets are elongate, with numerous fractures and dislocations (Fig. 6c), the quartz grains in the matrix show lobate morphology and chessboard extinction due to deformation. Prismatic sillimanite was verified by Raman spectroscopy (Fig. 6d), fibrolitic sillimanite occurs in the matrix intimately associated with biotite and muscovite. Inclusions of staurolite, rutile, ilmenite, biotite, white mica, sillimanite, quartz and monazite are located in the core of garnet (Fig. 7a,b). Some garnets are fractured, truncated or partially resorbed by biotite (often chloritized) at their margins and in pressure shadows, fractures are filled by chlorite (Fig. 7b,c).

Garnet porphyroblasts commonly show inclusion-rich cores and inclusion-free rims. Microprobe analyses performed along rim-core-rim profiles and compositional maps of selected grains show that garnet is zoned. In garnet from sample Ger1/17 (Fig. 8) there is a decrease in spessartine (X_{Sps}=0.21–0.17) and increase in pyrope (X_{Prp}=0.11–0.12) in its inclusion-rich core. A reverse pattern is observed in the inclusion-free rim (X_{Sps}=0.18; X_{Prp}=0.09). Garnet in sample VT1 (Fig. 9) shows similar compositional zoning with decreasing spessartine (X_{Sps}=0.14–0.08) and increasing pyrope (X_{Prp}=0.12–0.13) in the inclusion-rich core (see Fig. 7a,b) and highest spessartine (X_{Sps}=0.17) and lowest pyrope (X_{Prp}=0.07) in the rim. Compositional maps and patterns (Figs. 8, 9) indicate that prograde growth zonation of garnet was modified by diffusion (e.g. Spear 1991; Carlson 2006; Kohn & Spear 2000; Caddick et al. 2010). Patchy zonation of Ca with a network of

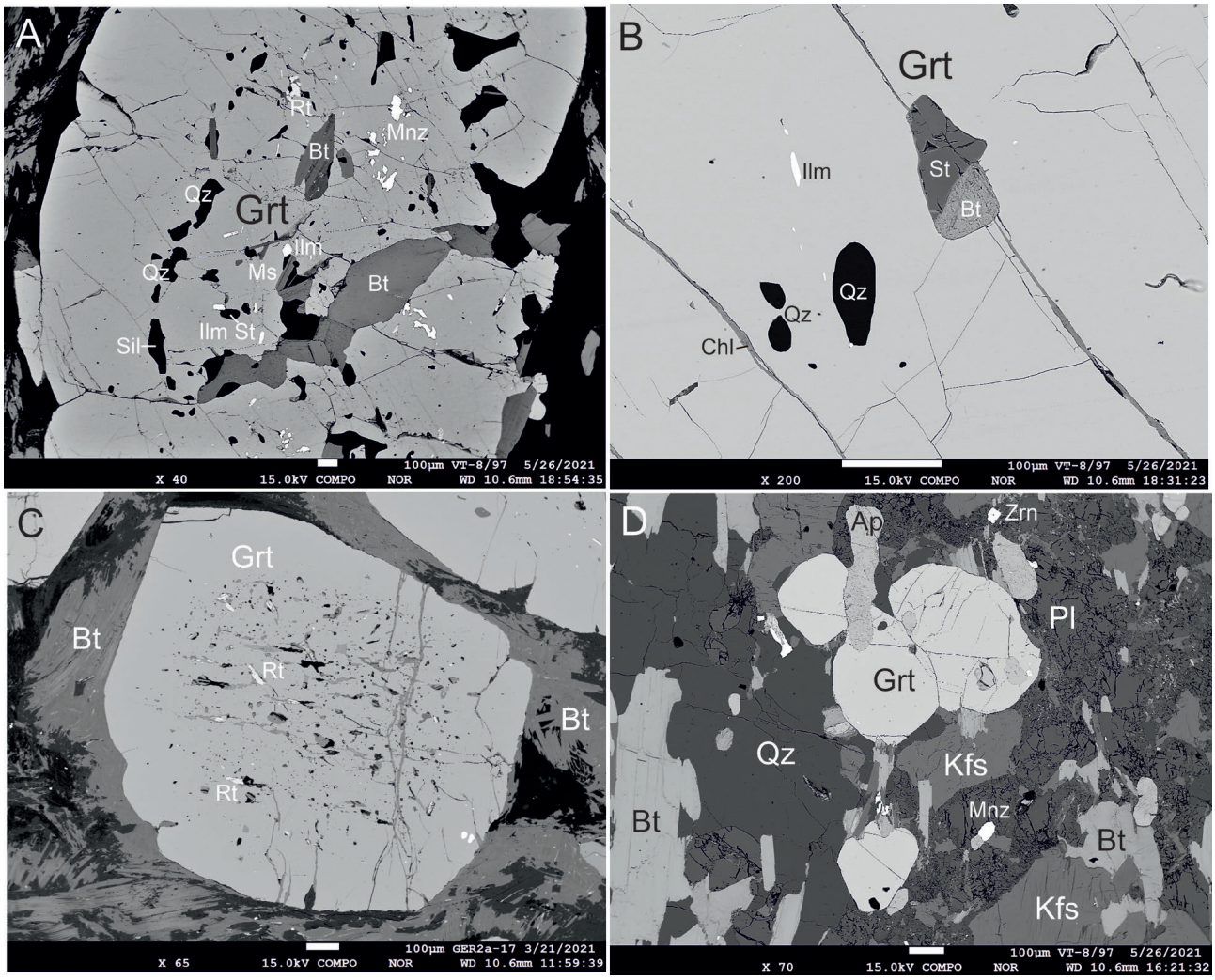

Fig. 7. BSE images of garnet in metapelitic gneiss and diatextite. **A** — Garnet porphyroblast in gneiss with inclusions of sillimanite, staurolite, rutile, ilmenite, muscovite, biotite, quartz and monazite. Sample VT1. **B** — Detail of staurolite, biotite, ilmenite and quartz inclusions in garnet. The microfracture is filled by chlorite. Sample VT1. **C** — Garnet porphyroblast in gneiss with inclusions of rutile among others. Microfractures penetrating the garnet are filled by chlorite and garnet rim is partly resorbed by biotite and chlorite due to retrogression. Sample Ger1/17. **D** — Euhedral garnets in the leucosome composed of K-feldspar, plagioclase and quartz. Remnants of original fabric are preserved by biotite palimpsests with abundant rounded apatites. Sample VT8/97.

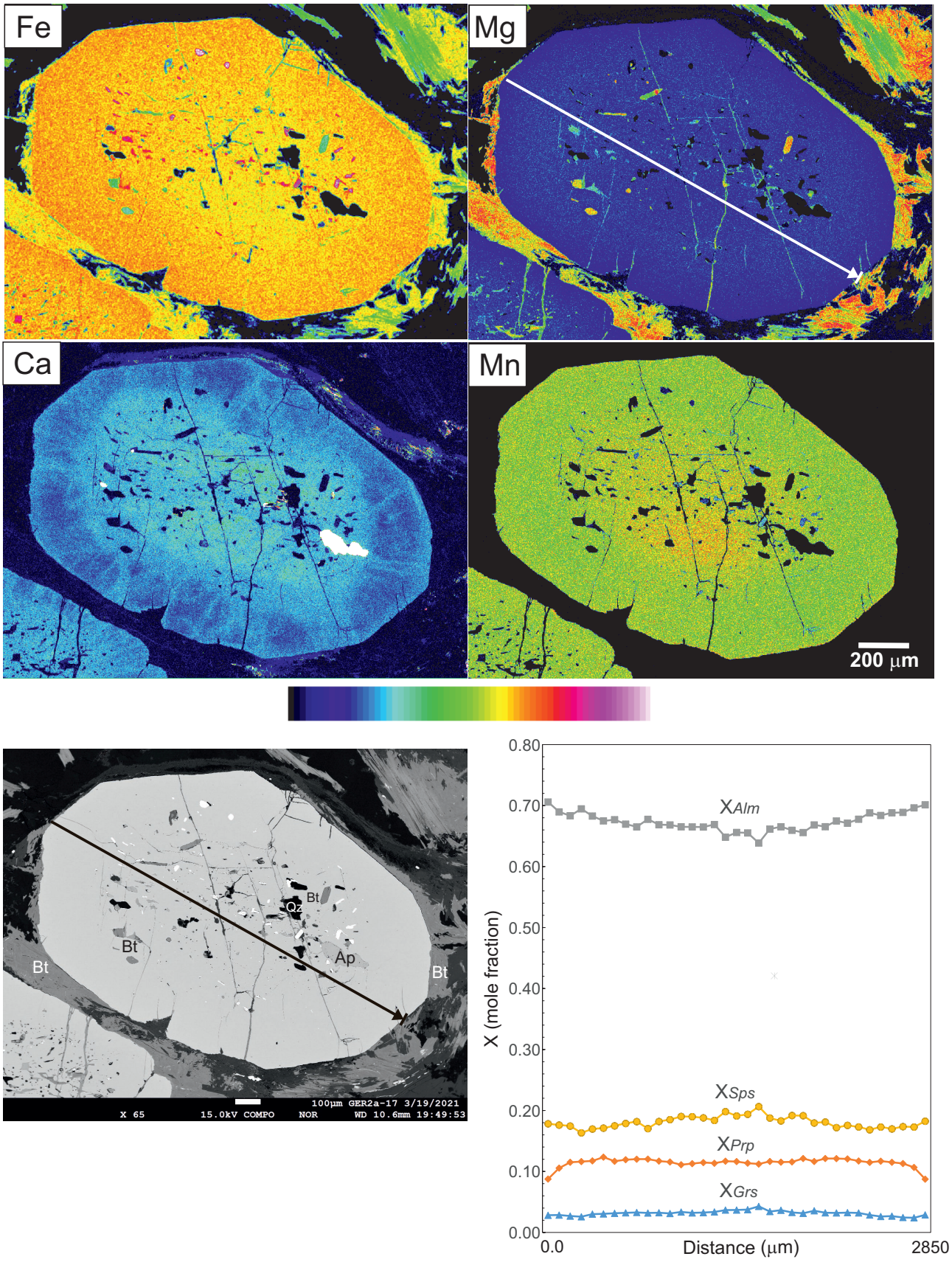

Fig. 8. Compositional maps, BSE image and a profile across garnet in metapelitic gneiss (Ger1/17).

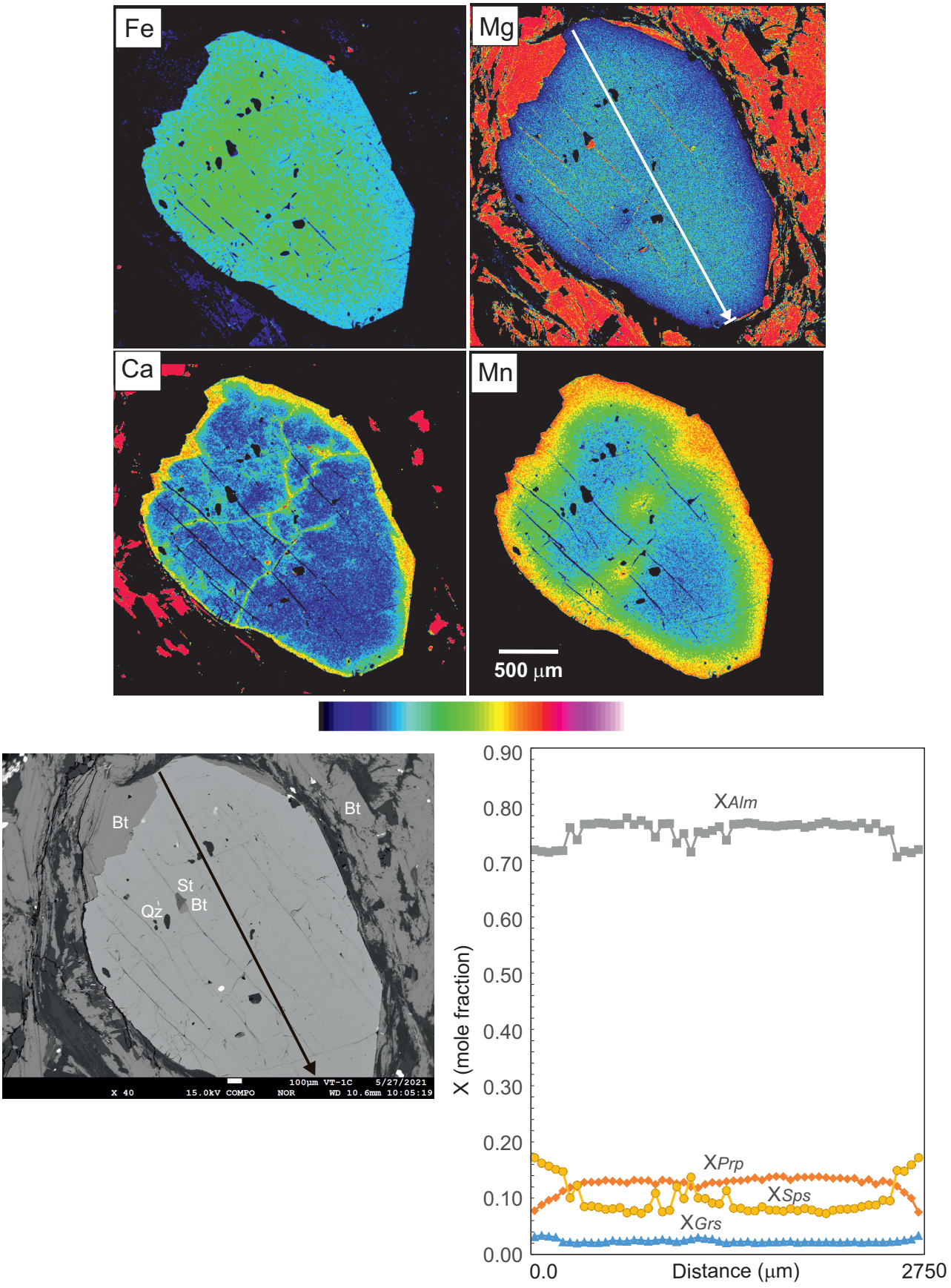

Fig. 9. Compositional maps, BSE image and a profile across garnet in metapelitic gneiss (VT1). Inclusions of staurolite, biotite and quartz are shown in detail in Fig. 7b.

microchannels is in contrast with the more concentric zonation of Fe, Mg and Mn. Ca distribution in garnet seems to be unrelated to fractures. These are filled by chlorite (Fig. 7b) and cross-cut the Ca domains or channels (Fig. 9), no sub-grains are visible in BSE images. There is a marked Mn enrichment in the rim of garnet in contact with biotite, especially in sample VT1 which shows that garnet is partly resorbed by biotite (Fig. 9). Such garnet resorption and Mn enrichment is commonly interpreted as a consequence of retrograde net-transfer reaction with biotite (Kohn & Spear 2000). According to Kohn & Spear (2000), Mn can be liberated to the matrix from partially dissolved garnet. Because biotite contains negligible Mn compared to garnet, Mn can increase on the rim of the garnet and diffuse back into the garnet. This implies that the highest-temperature part of the garnet remaining is reflected by the lowest Mn and minimum spessartine, and maximum pyrope composition of garnet may approximate peak metamorphic conditions. Representative analyses of garnet are in Table 1.

Biotite occurs as inclusions in garnet and in the matrix. Most biotite shows X_{Mg}=0.36–0.38 and TiO_2 content 2.9–3.5 wt% (Table 2). *White mica* porphyroblasts in the matrix correspond to muscovite with a moderate phengite component. Some inclusions in garnet show higher phengite content and paragonite was also detected (Table 3). Plagioclase ($An_{23–24}$) is present in the matrix (Table 4), no feldspar was found as inclusion in garnet. *Staurolite* enclosed in garnet is Fe-rich (X_{Fe}=0.81–86) with zinc content of 1–2.5 wt% (Table 5).

Migmatites

The rock texture is inhomogeneous, with segregations into leucosome, melanosome and/or mesosome. Stromatitic types, with recurrent leucocratic and melanocratic portions of the cm–dm thickness are most abundant, diatexites show larger portions of leucosome and less melanosome. The investigated samples (VT8/97, VT5/97) represent a garnet-bearing leucosome (Fig. 5) consisting of dominant felsic stripes composed of anhedral microcline and subhedral, sericitised plagioclase ($An_{12–35}$, typically An_{25}), see Table 4 for feldspars composition. Magnetite and Fe–Ti oxides occur as dark spots of mm size (Fig. 5). Remnants of original fabric are preserved by biotite palimpsests with abundant rounded apatites. Fibrolitic sillimanite is occasionally found within the felsic minerals. Minor and accessory minerals include apatite, zircon and monazite. Monazite*s* may be found both within felsic part enclosed by feldspars as well as in biotite.

Garnet occurs as small euhedral grains typically 0.25–1.3 mm in size (Figs. 7d, 10). These are free of inclusions or with inclusions of quartz, plagioclase, K-feldspar, apatite and zircon. Leucosome garnets are spessartine-rich. Compositional maps and profile (Fig. 10) show concentric zonation with Mn enrichment (X_{Sps}=0.22–0.28) and minor Mg (X_{Prp}=0.10–0.08) and Ca (X_{Grs}=0.05–0.04) depletion in a narrow rim compared to the core. Representative analyses of garnet are in Table 1.

Biotite shows X_{Mg}=0.34–0.36 and TiO_2=2.93–3.07 wt% composition (Table 2). *White mica* is muscovite with a higher Fe content (FeO=3.44–4.04 wt%; Table 3). *Ti-rich magnetite* (100–200 μm) is found in intergrowths with microcline and plagioclase, sometimes being overgrown by much larger pure *magnetite*, 1–2 mm in size (Fig. 11). Magnetite is commonly enclosed by fine-grained muscovite.

Granodiorite

Two-mica granodiorite is a medium-grained rock consisting of dominant eu- to subhedral zoned plagioclase ($An_{16–36}$), commonly sericitised or saussuritised (filled by small clinozoisite). Less abundant, finely perthitic and cross-hatched K-feldspar is represented by large anhedral grains enclosing plagioclase and micas. Mostly fresh dark-brown to pale-yellow biotite is commonly intergrown with muscovite. Some biotite is replaced by chlorite or epidote, muscovite often contains exsolutions of ores. Dominant accessory mineral is euhedral apatite (100–500 μm in size), usually enclosed by biotite, less common are small elongated zircons and Ti-magnetite grains. Monazite (50 μm) is mostly associated with biotite.

Thermodynamic modelling

The phase diagrams were calculated using Perple_X thermodynamic software (Connolly 2005: version 6.9.0) with internally consistent thermodynamic dataset (hp11ver.dat, TC-DS633) of Holland & Powell (2011). Solid-solution models for garnet, white mica, biotite, staurolite, cordierite, chlorite, magnetite, ilmenite, melt (White et al. 2014) and feldspar (Fuhrman & Lindsley 1988) were used, as available from the Perple_X datafile (solution_model.dat).

Metapelitic gneiss (Ger1/17)

The phase diagram (Fig. 12) was calculated in the system NCKFMMnASTH (Na_2O=0.36; CaO=0.32; K_2O=5.05; FeO=8.5; MgO=2.4; MnO=0.49; Al_2O_3=21.93; SiO_2=53.86; TiO_2=1.02 wt%) assuming H_2O fluid in excess, in the *P–T* range *T*=500–800 °C and *P*=1–10 kbar, based on our previous geothermobarometric results on High Tatra rocks (Janák et al. 1999). The bulk composition was determined from the XRF whole-rock analysis. Garnet composition was modelled as X_{Mg} [=Mg/(Mg+Fe+Ca+Mn)], X_{Fe} [=Fe/(Fe+Mg+Ca+Mn)], and X_{Mn} [=Mn/(Mg+Fe+Ca+Mn)] ratios. As pointed out above, maximum pyrope and minimum spessartine composition of garnet core was used to calculate peak metamorphic conditions. Biotite composition was modelled as X_{Mg} [=Mg/(Mg+Fe)] and feldspar as X_{Ca} [=Ca/(Ca+Na+K)], the composition of these phases in contrast to garnet is homogeneous (see Tables 1, 2 and 4). The calculated isopleths of garnet (X_{Mg}^{Grt}=0.12, X_{Fe}^{Grt}=0.67, X_{Mn}^{Grt}=0.17), biotite (X_{Mg}^{Bt}=0.38) and plagioclase (X_{Ca}^{Fsp}=0.23) plot within the stability field of garnet+sillimanite+plagioclase+biotite+muscovite+

Table 1: Representative microprobe analyses of garnet.

Sample	Ger1/17	Ger1/17	Ger1/17	VT1	VT1	VT1	VT10	VT10	VT10	VT8/97	VT8/97	VT5/21	VT5/21
Anal. point	core (maxSps)	core (maxPrp)	rim (minPrp)	core (maxSps)	core (maxPrp)	rim (minPrp)	core (maxSps)	core (maxPrp)	rim (minPrp)	core	rim	core	rim
SiO_2	36.82	36.95	36.53	36.16	36.35	36.49	36.41	36.33	36.33	36.34	36.33	35.853	36.034
TiO_2	0.01	0.03	0.04	0.01	0.00	0.03	0.03	0.02	0.00	0.03	0.02	0.056	0
Al_2O_3	21.16	21.18	21.00	21.23	21.22	20.94	21.02	21.34	21.13	20.77	20.77	20.858	20.781
Cr_2O_3	0.01	0.01	0.03	0.00	0.00	0.00	0.05	0.00	0.01	0.01	0.00	0	0
FeO^t	29.19	30.66	31.23	32.01	33.71	32.15	32.19	32.51	31.69	26.77	25.26	28.061	28.129
MnO	9.31	7.67	8.02	6.06	3.57	7.58	7.38	4.85	7.19	11.09	13.59	10.821	11.444
MgO	2.88	3.15	2.19	3.02	3.25	1.88	2.46	2.88	2.46	2.43	1.69	2.535	2.431
CaO	1.52	1.08	1.00	0.96	0.81	1.17	1.04	1.00	1.03	1.47	1.53	1.615	1.382
Total	100.95	100.75	100.16	99.58	99.08	100.34	100.57	98.94	99.85	99.02	99.23	99.799	100.201
Si	2.959	2.968	2.971	2.946	2.964	2.97	2.947	2.959	2.953	2.978	2.982	2.927	2.936
Ti	0.001	0.002	0.002	0.001	0	0.002	0.002	0.001	0.000	0.002	0.001	0.003	0.000
Al	2.005	2.006	2.014	2.039	2.04	2.01	2.005	2.049	2.025	2.006	2.01	2.007	1.996
Cr	0.001	0.001	0.002	0	0	0	0.003	0	0.001	0.001	0	0.000	0.000
Fe	1.962	2.06	2.124	2.181	2.299	2.189	2.179	2.215	2.154	1.835	1.734	1.916	1.917
Mn	0.634	0.522	0.553	0.418	0.247	0.523	0.506	0.335	0.495	0.77	0.945	0.748	0.790
Mg	0.345	0.377	0.265	0.367	0.395	0.228	0.297	0.35	0.299	0.297	0.207	0.308	0.295
Ca	0.131	0.093	0.087	0.084	0.071	0.102	0.09	0.088	0.09	0.129	0.135	0.141	0.121
Total	8.038	8.029	8.018	8.036	8.016	8.024	8.029	7.997	8.017	8.018	8.014	8.050	8.055
X_{Alm}	0.64	0.67	0.70	0.72	0.76	0.72	0.71	0.74	0.71	0.61	0.57	0.62	0.61
X_{Sps}	0.21	0.17	0.18	0.14	0.08	0.17	0.16	0.11	0.16	0.25	0.31	0.24	0.25
X_{Prp}	0.11	0.12	0.09	0.12	0.13	0.07	0.10	0.12	0.10	0.10	0.07	0.10	0.09
X_{Grs}	0.04	0.03	0.03	0.03	0.02	0.03	0.03	0.03	0.03	0.04	0.04	0.05	0.04

Structural formulae calculated on the basis of 12 oxygens.

Table 2: Representative microprobe analyses of biotite.

Sample	Ger1/17	Ger1/17	Ger1/17	Ger1/17	VT1	VT1	VT8/97	VT8/97	VT8/97	VT8/97
Position	Matrix	Matrix	Matrix	Matrix	in Grt/St	Matrix	Matrix	Matrix	Matrix	Matrix
SiO_2	35.10	35.41	35.33	35.57	34.69	34.88	34.57	34.84	34.81	34.43
TiO_2	3.47	3.18	3.22	2.91	3.40	3.28	3.07	3.05	3.25	2.93
Al_2O_3	18.23	18.45	18.94	18.57	17.05	18.03	16.69	17.05	18.22	17.23
Cr_2O_3	0.06	0.03	0.07	0.04	0.03	0.04	0.03	0.00	0.02	0.01
FeO^t	21.49	21.46	21.71	22.01	23.03	22.30	24.31	24.60	21.87	23.59
MnO	0.21	0.08	0.15	0.22	0.10	0.18	0.49	0.60	0.19	0.35
MgO	7.24	7.24	7.50	7.53	6.71	7.10	7.24	7.04	6.91	7.39
CaO	0.01	0.00	0.00	0.01	0.05	0.00	0.05	0.01	0.00	0.00
Na_2O	0.38	0.08	0.11	0.08	0.14	0.24	0.05	0.00	0.15	0.05
K_2O	9.42	9.67	9.72	9.78	9.47	9.56	9.68	9.97	9.61	9.94
F	0.31	0.00	0.22	0.22	0.04	0.05	0.29	0.25	0.00	0.05
Cl	0.06	0.07	0.07	0.08	0.12	0.11	0.04	0.05	0.08	0.03
H_2Ocalc	3.75	3.91	3.79	3.79	3.83	3.84	3.70	3.71	3.88	3.82
O=F	−0.13	0.00	−0.09	−0.09	−0.02	−0.02	−0.12	−0.10	0.00	−0.02
O=Cl	−0.01	−0.02	−0.01	−0.02	−0.03	−0.03	−0.01	−0.01	−0.02	−0.01
Total	99.59	99.55	100.71	100.69	98.60	99.56	100.06	101.06	98.98	99.81
Si	5.398	5.436	5.367	5.414	5.442	5.392	5.390	5.384	5.402	5.366
AlIV	2.602	2.564	2.633	2.586	2.558	2.608	2.610	2.616	2.598	2.634
T	8.000	8.000	8.000	8.000	8.000	8.000	8.000	8.000	8.000	8.000
AlVI	0.703	0.774	0.758	0.745	0.594	0.677	0.457	0.490	0.735	0.530
Ti	0.401	0.367	0.367	0.333	0.401	0.381	0.359	0.354	0.379	0.344
Fe^{2+}	2.764	2.755	2.757	2.802	3.021	2.882	3.169	3.179	2.838	3.074
Mn	0.028	0.011	0.019	0.028	0.013	0.023	0.064	0.079	0.025	0.046
Mg	1.661	1.657	1.699	1.710	1.570	1.635	1.684	1.622	1.598	1.717
Cr	0.007	0.004	0.008	0.005	0.004	0.005	0.004	0.000	0.003	0.001
Y	5.563	5.567	5.608	5.623	5.603	5.603	5.737	5.724	5.578	5.712
Ca	0.002	0.000	0.000	0.001	0.008	0.000	0.008	0.002	0.000	0.000
Na	0.113	0.024	0.031	0.022	0.042	0.073	0.015	0.000	0.045	0.014
K	1.848	1.893	1.883	1.898	1.895	1.886	1.925	1.965	1.902	1.977
Z	1.963	1.918	1.915	1.921	1.944	1.958	1.948	1.968	1.948	1.991
Total	15.526	15.485	15.523	15.544	15.548	15.561	15.685	15.691	15.525	15.703
F	0.151	0.000	0.107	0.104	0.021	0.022	0.142	0.120	0.000	0.026
Cl	0.016	0.018	0.017	0.020	0.032	0.030	0.011	0.013	0.022	0.008
OH	3.833	3.982	3.876	3.876	3.947	3.948	3.847	3.866	3.978	3.966
anions	4.000	4.000	4.000	4.000	4.000	4.000	4.000	4.000	4.000	4.000
X_{Mg}	0.38	0.38	0.38	0.38	0.34	0.36	0.35	0.34	0.36	0.36

Structural formulae calculated on the basis of 22 oxygens.

Table 3: Representative microprobe analyses of white mica.

Sample	Ger1/17	Ger1/17	Ger1/17	Ger1/17	VT1	VT8/97	VT8/97	VT8/97
Mineral	Ph	Pg	Ms	Ms	Ms	Ms	Ms	Ms
Position	in Grt	in Grt	Matrix	Matrix	Matrix	Matrix	Matrix	Matrix
SiO_2	52.07	51.02	46.68	46.65	45.44	45.81	45.49	45.89
TiO_2	0.11	0.05	0.93	0.73	1.01	1.45	1.22	0.98
Al_2O_3	27.60	33.74	34.65	36.08	33.63	31.25	32.83	33.41
Cr_2O_3	0.00	0.00	0.06	0.05	0.01	0.03	0.01	0.01
FeO^t	3.69	1.68	1.57	1.16	2.30	3.44	4.04	3.87
MnO	0.21	0.21	0.03	0.00	0.11	0.02	0.00	0.01
MgO	2.40	0.69	0.27	0.20	0.26	0.40	0.72	0.66
CaO	0.02	0.07	0.00	0.00	0.01	0.03	0.01	0.03
Na_2O	0.10	3.41	0.47	0.53	0.55	0.14	0.28	0.43
K_2O	10.16	3.60	10.63	10.24	9.94	11.21	10.86	10.69
F	0.16	0.00	0.04	0.04	0.00	0.05	0.00	0.00
Cl	0.01	0.01	0.00	0.00	0.00	0.00	0.01	0.01
H_2Ocalc	4.42	4.67	4.49	4.51	4.50	4.41	4.43	4.44
O=F	−0.07	0.00	−0.02	−0.02	0.00	−0.02	0.00	0.00
O=Cl	0.00	0.00	0.00	0.00	0.00	0.00	0.00	0.00
Total	100.89	99.16	99.79	100.16	97.74	98.21	99.90	100.42
Si	6.878	6.600	6.222	6.162	6.204	6.304	6.158	6.163
AlIV	1.122	1.400	1.778	1.838	1.796	1.696	1.842	1.837
T	8.000	8.000	8.000	8.000	8.000	8.000	8.000	8.000
AlVI	3.175	3.744	3.665	3.779	3.615	3.372	3.395	3.451
Ti	0.011	0.005	0.094	0.072	0.103	0.150	0.124	0.099
Fe^{2+}	0.407	0.182	0.175	0.128	0.262	0.396	0.457	0.435
Mn	0.024	0.023	0.004	0.000	0.012	0.002	0.000	0.002
Mg	0.472	0.134	0.053	0.040	0.052	0.083	0.146	0.131
Cr	0.000	0.000	0.006	0.005	0.001	0.003	0.001	0.001
Y	4.090	4.088	3.996	4.024	4.047	4.005	4.123	4.118
Ca	0.003	0.009	0.000	0.000	0.001	0.004	0.002	0.004
Na	0.026	0.856	0.121	0.135	0.147	0.036	0.075	0.113
K	1.713	0.595	1.808	1.726	1.731	1.968	1.875	1.831
Z	1.742	1.460	1.929	1.861	1.879	2.009	1.951	1.948
Total	13.832	13.548	13.924	13.885	13.925	14.013	14.073	14.066
F	0.067	0.000	0.016	0.018	0.000	0.024	0.000	0.000
Cl	0.003	0.002	0.001	0.000	0.000	0.000	0.003	0.002
OH	3.930	3.998	3.983	3.982	4.000	3.976	3.997	3.998
anions	4.000	4.000	4.000	4.000	4.000	4.000	4.000	4.000

Structural formulae calculated on the basis of 22 oxygens.

Table 4: Representative microprobe analyses of feldspar.

Sample	Ger1/17	Ger1/17	VT1	VT10	VT8/97	VT8/97	VT8/97	VT8/97
Mineral	Pl	Pl	Pl	Pl	Pl	Pl	Pl	Kfs
SiO_2	62.64	63.05	61.95	61.53	62.78	61.87	61.61	63.61
Al_2O_3	23.89	23.89	24.08	24.27	23.74	24.17	24.35	18.81
CaO	4.86	4.74	4.91	5.28	4.68	5.18	5.38	0.02
Na_2O	8.70	8.78	8.50	8.50	8.67	8.53	8.35	0.30
K_2O	0.13	0.09	0.08	0.18	0.27	0.26	0.28	16.39
Total	100.21	100.55	99.52	99.77	100.13	100.01	99.97	99.12
Si	2.765	2.772	2.753	2.731	2.773	2.743	2.733	2.972
Al	1.243	1.238	1.261	1.270	1.236	1.263	1.274	1.036
Ca	0.230	0.223	0.234	0.251	0.221	0.246	0.256	0.001
Na	0.745	0.748	0.732	0.732	0.742	0.733	0.718	0.027
K	0.007	0.005	0.005	0.010	0.015	0.015	0.016	0.977
Total	4.990	4.986	4.985	4.994	4.987	5.000	4.997	5.013
X_{Ca}	0.23	0.23	0.24	0.25	0.23	0.25	0.26	0.00
X_{Na}	0.76	0.77	0.75	0.74	0.76	0.74	0.73	0.03
X_K	0.01	0.01	0.01	0.01	0.02	0.02	0.02	0.97

Structural formulae calculated on the basis of 8 oxygens.

ilmenite+quartz, which is the peak metamorphic assemblage for the rock. The intersecting isopleths constrain the peak *P–T* values to 5–6 kbar and 650–700 °C, below the wet solidus (Fig. 12).

Migmatite leucosome (VT8/97)

The leucosome was modelled as crystallizing melt rather than as a metamorphic rock in the system NCKFMMnASTH (SiO_2=74.03, TiO_2=0.09, Al_2O_3=14.59, FeO=0.86, MnO=0.02, MgO=0.16, CaO=1.22, Na_2O=2.46, K_2O=5.92 wt%). The amount of water necessary to obtain melt was estimated using pseudosection *T* vs. H_2O wt% at 5 kbar (Fig. 13), the nominal pressure derived by modelling the metapelitic gneiss Ger1/17 (Fig. 12). Supposing that biotite and garnet are in equilibrium, isopleths of TiO_2 in biotite (3–3.5 wt%) and X_{Ca}=0.045 in garnet intersect at 750–780 °C and 7 wt% H_2O (Fig. 13). Since the leucosome is characterized by the presence of magnetite and Fe–Ti oxides, the latter have been used for calculations of temperature and oxygen fugacity. These were then calculated using the procedures of Ghiorso & Evans (2008) and Anderson & Lindsley (1985). The temperature obtained according to both calibrations is 760–772 °C; oxygen fugacity is log f_{O2}=−15.6 and −16.6, respectively. Hence, the *P–T* pseudosection on Fig. 14 was calculated using 7 wt% H_2O and oxygen fugacity controlled at log f_{O2}=−16, in the *P–T* window *T*=600–800 °C and *P*=1–10 kbar. The observed primary mineral assemblage plagioclase+K-feldspar+quartz+garnet+sillimanite+biotite+ilmenite plots above the wet solidus between 4.5–8 kbar and 700–770 °C. Biotite isopleths (TiO_2=3.0 and 3.4 wt%) constrain the temperature at 760–770 °C. The maximum temperature derived by the Fe–Ti oxides is 770 °C, in the range constrained by the biotite TiO_2 isopleths at 7.5 kbar. The presence of pure magnetite with voids (Fig. 10) coexisting with muscovite indicates cooling below 5.5 kbar and 640 °C (Fig. 14).

Table 5: Representative microprobe analyses of staurolite.

Sample	VT1	VT1	VT10
Position	in Grt	in Grt	in Grt
SiO_2	25.20	24.98	25.17
TiO_2	0.76	0.60	0.72
Al_2O_3	55.20	55.30	55.33
Cr_2O_3	0.13	0.09	0.08
FeO	12.14	13.63	11.48
MnO	0.20	0.25	0.39
MgO	1.46	1.77	1.05
ZnO	2.01	1.01	2.48
Na_2O	0.11	0.08	0.17
Total	97.19	97.70	96.86
Si	7.404	7.32	7.419
Ti	0.168	0.132	0.160
Al	19.114	19.099	19.224
Cr	0.029	0.02	0.020
Fe	2.982	3.339	2.829
Mn	0.05	0.061	0.097
Mg	0.639	0.775	0.459
Zn	0.435	0.218	0.540
Na	0.061	0.047	0.097
Total	30.882	31.011	30.843
X_{Fe}	0.82	0.81	0.86

Structural formulae calculated on the basis of 46 oxygens.

Monazite

Monazite occurrence

Monazite in the sample Ger1/17 occurs typically in the matrix, commonly forming strings of small anhedral grains 40–80 μm in size associated with biotite and muscovite (Fig. 15a,b). In a single case it was found enclosed within garnet at the outer boundary of the core. The strings and clusters follow foliation of the gneiss. Monazites from VT1 sample occur in clusters mostly within biotite flakes, ranging in size from 10 to 80 μm. They are rounded in contrast to anhedral inclusions found in garnet reaching up to 150 μm in length (Fig. 15c,d). Leucosome VT8/97 has typically rounded monazites up to 75 μm in size are found mostly in feldspars and quartz, less within biotite (Fig. 15e,f). The composition of monazite shown in Fig. 15 is presented in Table 6.

Monazite compositions

Monazites follow the monazite–cheralite substitution line consisting of 85–95 mol% of pure monazite and 15 mol% of cheralite. Xenotime and huttonite add 1–7 mol% and <1 mol%, respectively. The sample Ger1/17 monazite splits into two groups, the low Y and high Y groups of Ger1/17 sample have <3 mol% and 3.5–4.2 mol% of xenotime, respectively. The general picture of monazite compositions is shown in mnz–xno–cher end member triangle plot in Fig. 16a. The samples are arranged according to increasing xenotime from low-Y metapelite Ger1/17 to metapelites VT1, high Y Ger1/17, and VT8/97 with maximum content of xenotime. The range of cheralite is larger, the highest for low Y monazite in Ger1/17 sample, and the lowest for high Y monazite in the same sample (Ger1/17). The low and high Y varieties of the monazite in Ger/17 differ also by Ca and Si contents, and REE patterns. The older, low Y monazite is more heterogenous with a spread of middle and heavy REEs, Th and Ca. The VT8/97 shows the highest Y and the highest Si shifting the substitution trend distinctly to huttonite (Fig. 16b). The last sample VT1 is similar to sample Ger1/17 with intermediate xenotime contents, while it shows no distinction in Y contents. Both samples, VT1 and Ger1/17 also have the highest ThO_2 – up to 7–13 wt%. The REE distribution patterns are compared in Fig. 17. Two groups of Ger1/17 monazite show that while the younger, high Y monazite forms a more homogeneous group with narrow spread of the REEs, the older, low Y group is more heterogeneous in all HREE. Leucosome VT8/97 has homogeneous monazites with large negative anomalies (Fig. 17d). The metapelite VT1 contains monazites both in the matrix and enclosed in garnet. Figure 17c shows that monazite

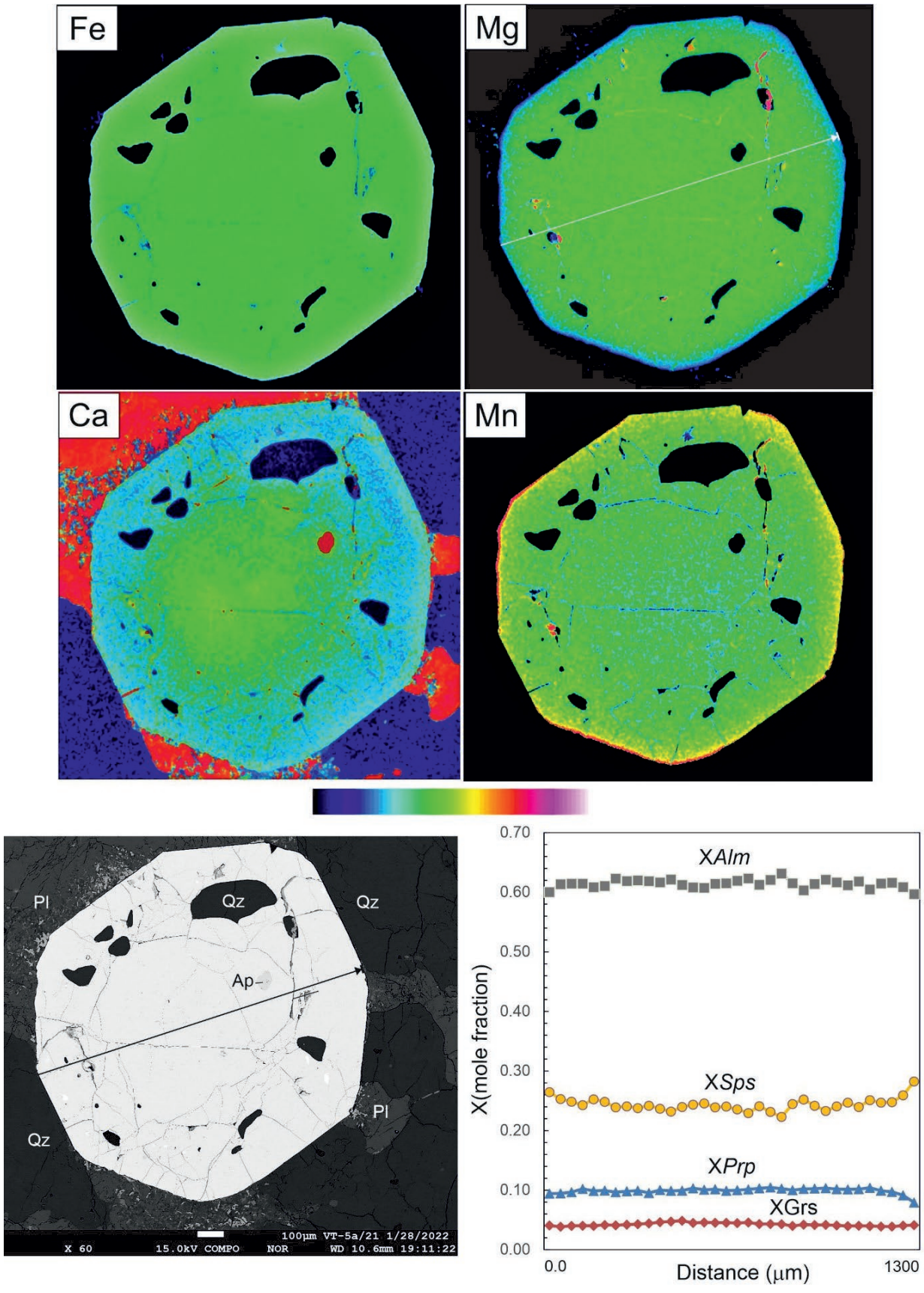

Fig. 10. Compositional maps, BSE image and a profile across garnet in diatexite leucosome (VT5/21).

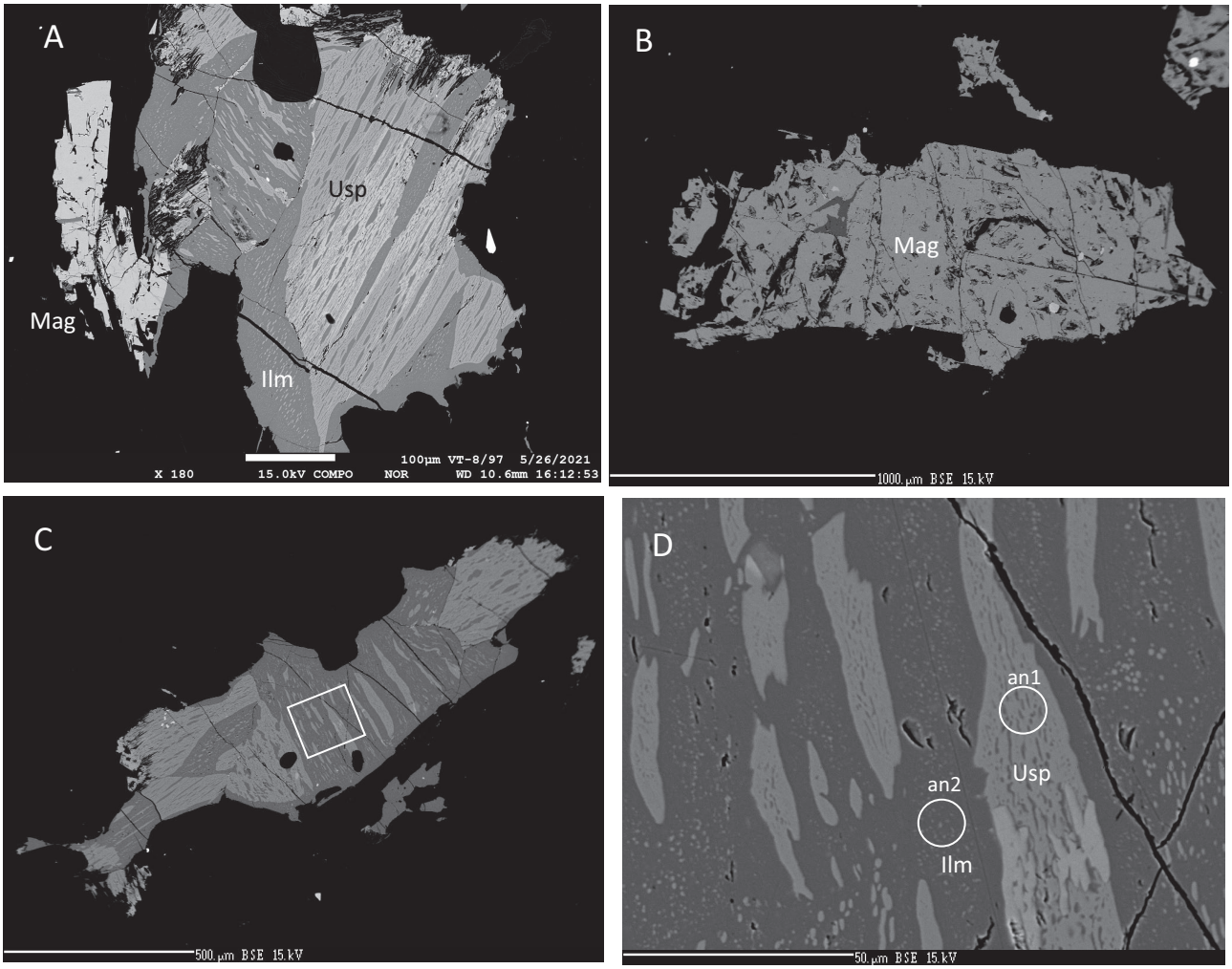

Fig. 11. BSE images of Fe–Ti oxides in the sample VT8/97. **A** — Ti-magnetite showing exsolutions of ilmenite from ulvöspinel (Usp) and magnetite from ilmenite (Ilm). Pure magnetite grows on the left. **B** — A large grain of pure magnetite showing voids. **C** — The grain of Ti-magnetite used for oxythermobarometry, the white quadrangle with analysed areas is shown in detail in (**D**).

in garnet is more homogeneous and has less pronounced negative Eu anomalies. There is no significant difference in Y contents between these monazites. Some analyses from VT1 and Ger1/17 monazites show distinctly lower La_N/Ce_N ratios and flatter LREE patterns. These analyses correspond to the high ThO_2 points and negative correlations between La, Ce vs Th indicates that Th substitutes mostly for these light REEs.

Monazite dating

Monazite was dated by the MARC (monazite age reference correction) method developed in the Dionýz Štúr State Geological Institute in Bratislava (Konečný et al. 2018), using microprobe analyses from CAMECA SX 100. Spot monazite analyses were acquired with conditions of 15 kV accelerating voltage, 180 nA beam current, and 3 µm beam diameter with the aim of increasing counting both efficiency and spatial resolution. Long counting times were used to increase analytical precision: for Pb – 300 s peak and 2×150 s backgrounds, Th – 35 s peak and 2×17.5 s background, U – 80 s peak and 80 s background, Y – 40 s peak and 2×20 s background. Calibration reference materials of REE's and Y were phosphates synthesized by Daniel Harlov at the GFZ German Research Centre, Potsdam, Germany: Pb – $PbCO_3$, Th – ThO_2, U – UO_2, S – barite, Ca – wollastonite, Sr – $SrTiO_3$, Al – Al_2O_3, Si – wollastonite and Fe – fayalite. Sequential measurement on the spectrometer in the order Pb, Th, U, Y (large PET) was corrected for acquisition time of these elements. Naturally curved background at Pb-Mα was estimated by a novel method (Konečný et al. 2018). Mutual interferences were resolved by an empirical correction, which included matrix effects on both reference material and on unknown sample. Age estimates were tested on monazites dated by methods of isotopic ratios of Pb and U, called age reference materials (ARM). A set of 10 ARM's was utilized for the assessment of minor systematic errors that cannot be suppressed in the currently used measuring procedure, but they are accumulated regardless of

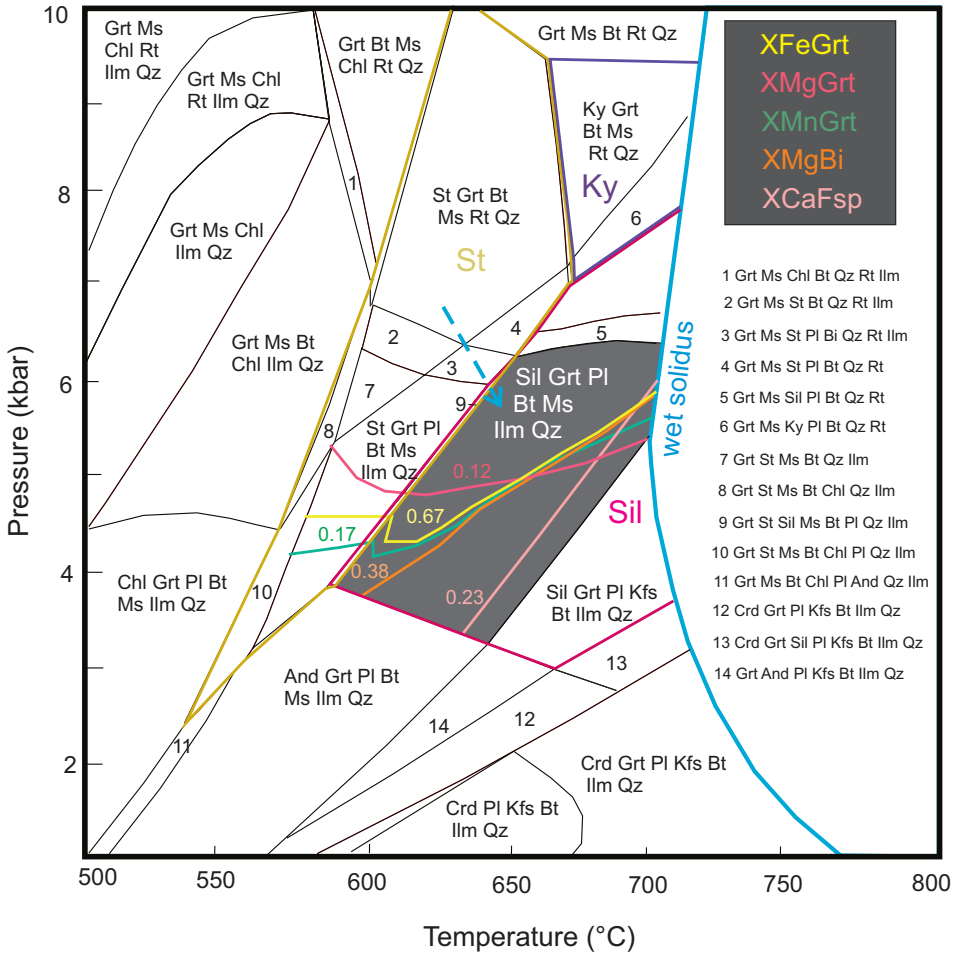

Fig. 12. Phase diagram (*P–T* section) for metapelitic metapelitic gneiss (Ger1/17) calculated using the thermodynamic data, mineral compositions and conditions described in the text. The shaded area shows the stability field of peak metamorphic assemblage and relevant compositions of garnet, biotite and plagioclase (isopleths). Staurolite-sillimanite sequence (dashed arrow) is discussed in the text.

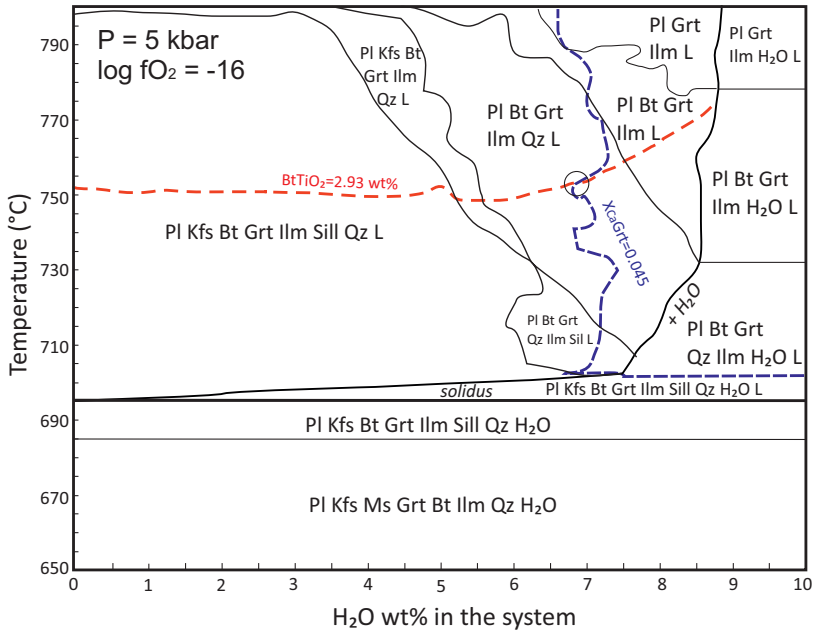

Fig. 13. Phase diagram (*T* vs. H_2O wt% section) for the sample VT8/97 at 5 kbars and oxygen fugacity log f_{O2}=−16. Biotite TiO_2= 2.93 wt% intersects with garnet X_{Ca}=0.045 at 7 wt% H_2O.

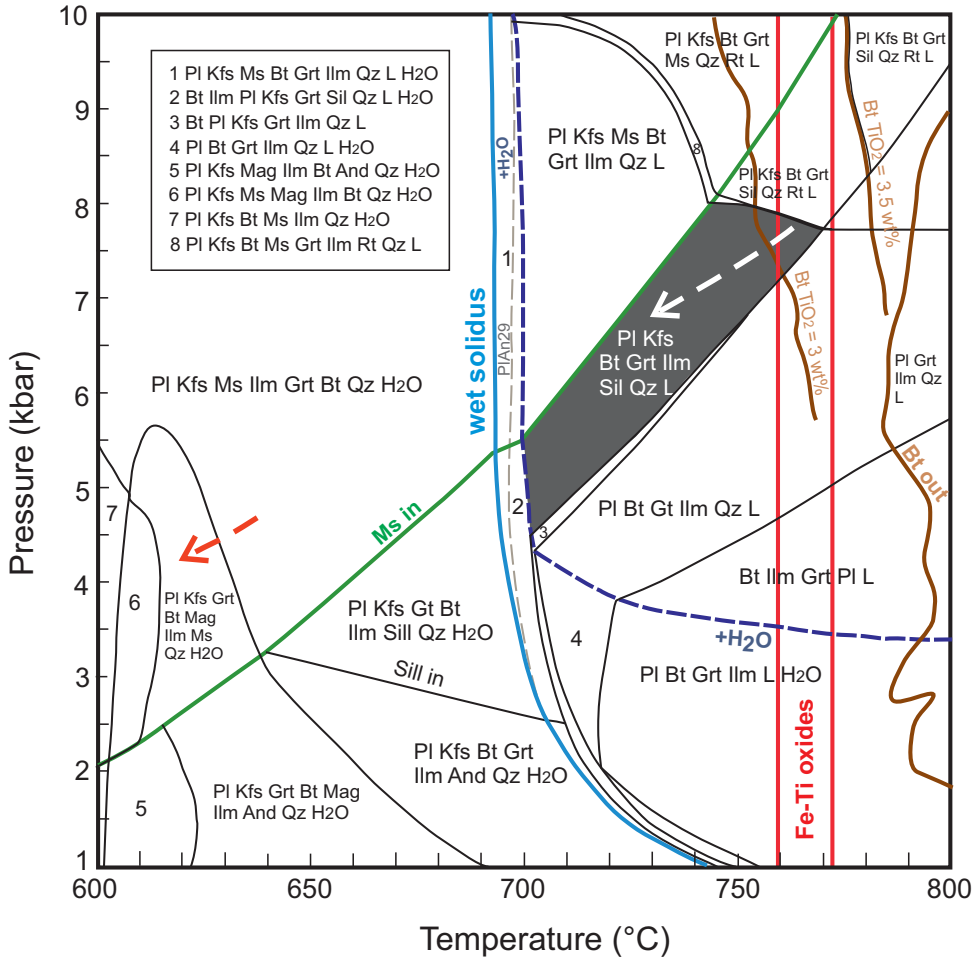

Fig. 14. Phase diagram (*P–T* section) for diatexite leucosome (VT8/97) calculated using the thermodynamic data, mineral compositions and conditions described in the text. The shaded area shows the stability field of primary mineral assemblage above solidus. Results of oxythermobarometry from Fe–Ti oxides coupled with biotite TiO_2 isopleths constrain the peak temperature. Cooling from peak conditions is marked by dashed red arrow. See the text for more details.

the number of analyses. Other details and principles of MARC dating technique are published in Konečný et al. (2018).

Monazites from two samples of metapelitic gneiss (Ger1/17, VT1), one leucosome of diatexite (VT8/97), and one sample of granodiorite (T8) described above were dated. In metapelitic gneisses and migmatite, 52 monazite crystals were measured, yielding 148 individual ages. The points with apparent ages <300 Ma and >379 Ma were excluded, and the rest, 128 points, was then recalculated by the method of Cocherie & Albarede (2012) using U/Pb vs. Th/Pb isochrons (Fig. 18) or as weighted average using Isoplot (Ludwig 2001, Table 7).

The metapelite sample VT1 (Fig. 18) yielded the age 348.5±4 Ma from a homogeneous set of individual ages with MSWD=0.36. The metapelite sample Ger1/17 (Fig. 18) has a slightly higher age and the line fitted from 33 points coincides with the error envelope indicating a heterogeneous population. Confronting the individual ages with Y contents of monazite shows that the population consists of two groups with differing Y contents. The low and high Y groups have averages 0.83 wt% and 1.47 wt% Y, respectively. The U/Pb vs. Th/Pb isochrons of these groups (Fig. 18) give different ages, 356.5 Ma for the low Y, and 345.8 Ma for the high Y group with fitted lines close to the isochrons. The Gerlach sample, therefore, seems to has preserved two ages from two stages of metamorphic evolution differing in Y contents. The leucosome VT8/97 provides a homogeneous set of individual ages giving weighted average of 351.5 Ma with MSWD 0.36. Dating of monazite (62 points) in two-mica granite (sample T8) yielded the weighted average of 349.7±4 Ma. The MSWD =1.3 indicates some disturbance of the system but the subdivision is not supported by any chemical or textural features. All analysed points are given in Electronic Suppl. Table S1.

Discussion

Prograde staurolite-sillimanite sequence

Metapelitic gneisses and migmatites of the Tatra Mountains comprise several reaction textures which, together with

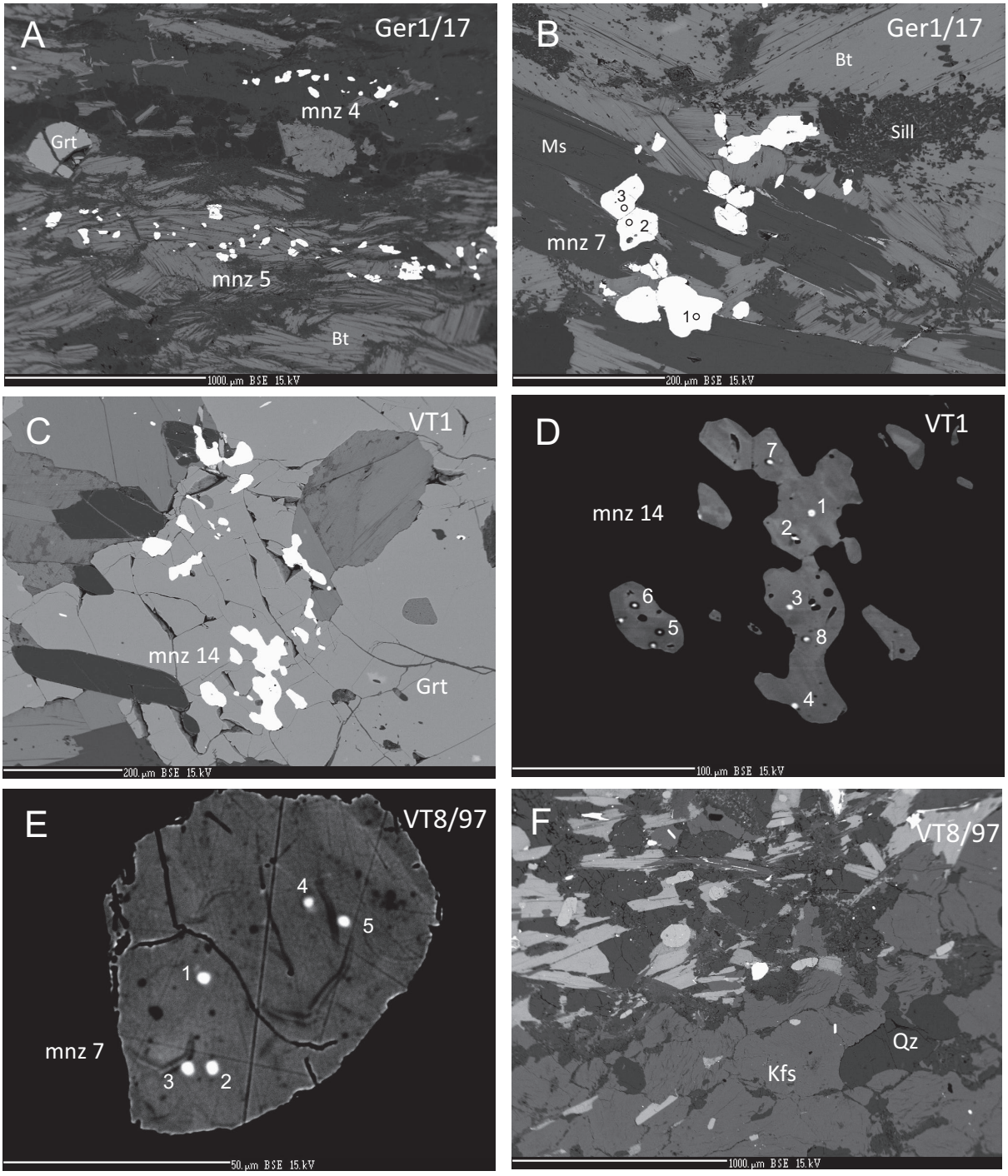

Fig. 15. BSE images of the dated monazites occurring in various textural positions. Numbers refer to point analyses (see Table 6).

evidence of partial melting and deformation/crystallisation relationships of mineral assemblages, have been used to constrain their evolution and *P–T* path. In metapelitic gneisses, staurolite inclusions in the garnets and the presence of sillimanite both as inclusions in garnet and in the matrix reflect staurolite elimination by the reaction

staurolite+muscovite+quartz=garnet+sillimanite+biotite $+H_2O$ (R1)

during increasing temperature. As demonstrated by mineral assemblages in the phase equilibrium diagram (Fig. 12), inclusions of rutile, phengitic muscovite and paragonite in the garnet core may indicate an earlier metamorphic stage in the stability field of rutile (Rt in) above 6 kbars. Calculated peak metamorphic conditions of gneiss are 5–6 kbar and 650–700 °C, within the stability field of garnet+sillimanite+plagioclase+biotite+muscovite+ilmenite+quartz. Hence a *P–T* path (dashed arrow) from the (St, Grt, Bt, Ms, Rt, Qz) stability

field at increasing temperature and decreasing pressure was likely.

Patchy zonation of Ca with a network of microchannels in garnet is similar to microtextures observed in high-pressure rocks (e.g. Konrad-Schmolke et al. 2007; Giuntoli et al. 2018; Bukala et al. 2020). These have been interpreted as a selective compositional re-equilibration along the sub-grain boundaries (Konrad-Schmolke et al. 2007), fracturing-healing process due to interaction with fluid in polymetamorphic garnet (Giuntoli et al. 2018), or migration pathways of fluid derived by a breakdown of hydrous phase inside garnet (Bukala et al. 2020). As pointed out above, Ca distribution in garnet seems to be unrelated to fractures or sub-grains, decomposition of Ca-rich hydrous phase remains uncertain and more detailed study is needed.

Prograde metamorphic sequence of Barrovian type with staurolite+kyanite+sillimanite-bearing assemblages was observed in metapelitic micaschists of the lower unit (staurolite+kyanite zone; kyanite–fibrolite zone) and paragneisses and migmatites of the upper unit (kyanite zone) in the Western Tatra (Fig. 2), described in more detail previously (Janák 1994; Janák et al. 1988, 1999). In the kyanite zone metapelites,

Table 6: Microprobe analyses and structural formulae of selected monazites shown in Fig. 14.

	Ger1/17					VT1								VT8/97			
Note	**high Y**	**high Y**	**high Y**	**low Y**	**low Y**												
Fig.:	**15B**	**15B**	**15B**			**15D**	**15D**	**15D**	**15D**	**15D**	**15D**	**15D**	**15D**	**15E**	**15E**	**15E**	**15E**
point	**m7/1**	**m7/2**	**m7/3**	**m4/2**	**m4/5**	**m14/1**	**m14/2**	**m14/3**	**m14/4**	**m14/5**	**m14/6**	**m14/7**	**m14/8**	**m7/1**	**m7/2**	**m7/3**	**m7/4**
SiO_2	0.19	0.16	0.16	0.39	0.22	0.31	0.57	0.31	0.18	0.18	0.39	0.31	0.32	0.52	0.73	0.57	0.36
FeO	0.00	0.01	0.00	0.15	0.00	0.09	0.40	0.27	1.22	0.50	0.40	0.20	0.26	0.00	0.00	0.00	0.00
CaO	1.11	1.19	1.23	1.40	0.74	1.50	2.12	1.01	0.57	0.57	1.15	1.27	1.04	0.56	0.61	0.50	0.32
SrO	0.03	0.01	0.02	0.02	0.01	0.03	0.02	0.02	0.00	0.02	0.03	0.01	0.03	0.00	0.01	0.00	0.01
UO_2	0.51	0.85	0.80	0.34	0.40	0.35	0.16	0.12	0.19	0.17	0.21	0.29	0.13	0.30	0.71	0.29	0.27
P_2O_5	30.44	30.16	30.16	29.56	29.82	29.05	28.77	29.07	29.39	29.78	29.14	29.33	29.35	29.60	29.20	29.44	29.67
PbO	0.10	0.12	0.11	0.12	0.08	0.12	0.09	0.08	0.05	0.05	0.10	0.11	0.08	0.06	0.09	0.06	0.04
La_2O_3	14.01	13.54	13.73	11.26	15.09	10.41	9.70	11.73	15.21	14.27	13.76	10.81	11.86	11.78	11.66	12.20	12.34
Ce_2O_3	28.57	28.02	28.16	29.65	30.67	27.90	29.00	30.26	30.11	30.83	29.17	28.67	30.39	27.02	25.77	27.33	28.10
Pr_2O_3	3.00	2.96	2.91	3.29	3.15	3.37	3.52	3.49	3.09	3.34	3.03	3.40	3.44	3.35	3.22	3.38	3.41
Nd_2O_3	10.64	10.50	10.29	11.39	10.81	11.99	13.25	12.35	10.73	11.38	10.59	12.31	11.88	13.62	13.40	13.66	13.84
Sm_2O_3	1.85	1.84	1.77	1.44	1.74	1.84	2.06	1.79	1.70	1.73	1.53	1.87	1.69	2.68	2.75	2.76	2.77
Eu_2O_3	0.04	0.15	0.12	0.24	0.15	0.13	0.14	0.17	0.23	0.22	0.18	0.15	0.14	0.07	0.00	0.07	0.12
Gd_2O_3	1.38	1.28	1.36	0.53	0.94	0.93	1.09	0.96	0.97	0.97	0.95	1.17	0.99	1.98	2.25	1.91	2.02
Tb to Lu	2.25	2.05	2.18	1.14	1.33	1.35	1.05	1.06	1.07	1.10	0.96	1.21	1.13	2.11	2.52	1.95	2.10
ThO_2	4.72	4.67	4.96	7.32	3.32	7.49	7.31	5.62	2.87	2.85	6.48	6.71	5.85	3.89	4.46	3.91	2.15
Y_2O_3	2.03	1.87	1.97	0.83	0.55	1.72	0.85	1.11	1.18	1.32	1.07	1.64	1.11	2.44	3.06	2.27	2.40
Total	100.87	99.39	99.93	99.07	99.01	98.57	100.09	99.43	98.77	99.26	99.16	99.44	99.71	99.98	100.45	100.32	99.92
P	0.996	0.999	0.996	0.989	0.997	0.982	0.962	0.978	0.986	0.992	0.980	0.982	0.982	0.982	0.969	0.977	0.986
Si	0.007	0.006	0.006	0.015	0.009	0.012	0.022	0.012	0.007	0.007	0.015	0.012	0.013	0.020	0.029	0.023	0.014
Ca	0.046	0.050	0.051	0.059	0.031	0.064	0.090	0.043	0.024	0.024	0.049	0.054	0.044	0.024	0.026	0.021	0.013
Sr	0.001	0.000	0.000	0.001	0.000	0.001	0.000	0.001	0.000	0.001	0.001	0.000	0.001	0.000	0.000	0.000	0.000
Fe	0.000	0.000	0.000	0.005	0.000	0.003	0.013	0.009	0.040	0.016	0.013	0.007	0.009	0.000	0.000	0.000	0.000
Th	0.041	0.042	0.044	0.066	0.030	0.068	0.066	0.051	0.026	0.026	0.059	0.060	0.053	0.035	0.040	0.035	0.019
U	0.004	0.007	0.007	0.003	0.004	0.003	0.001	0.001	0.002	0.001	0.002	0.003	0.001	0.003	0.006	0.003	0.002
Pb	0.001	0.001	0.001	0.001	0.001	0.001	0.001	0.001	0.001	0.001	0.001	0.001	0.001	0.001	0.001	0.001	0.000
La	0.200	0.195	0.198	0.164	0.220	0.153	0.141	0.172	0.222	0.207	0.201	0.158	0.173	0.170	0.169	0.176	0.179
Ce	0.404	0.401	0.402	0.429	0.443	0.408	0.419	0.440	0.437	0.444	0.424	0.415	0.440	0.388	0.370	0.392	0.404
Pr	0.042	0.042	0.041	0.047	0.045	0.049	0.051	0.051	0.045	0.048	0.044	0.049	0.049	0.048	0.046	0.048	0.049
Nd	0.147	0.147	0.143	0.161	0.152	0.171	0.187	0.175	0.152	0.160	0.150	0.174	0.168	0.191	0.188	0.191	0.194
Sm	0.025	0.025	0.024	0.020	0.024	0.025	0.028	0.025	0.023	0.023	0.021	0.025	0.023	0.036	0.037	0.037	0.038
Eu	0.000	0.002	0.002	0.003	0.002	0.002	0.002	0.002	0.003	0.003	0.002	0.002	0.002	0.001	0.000	0.001	0.002
Gd	0.018	0.017	0.018	0.007	0.012	0.012	0.014	0.013	0.013	0.013	0.013	0.015	0.013	0.026	0.029	0.025	0.026
Tb to Lu	0.0272	0.0252	0.0266	0.0142	0.0165	0.017	0.0131	0.0134	0.0133	0.0137	0.0121	0.0151	0.014	0.0262	0.0313	0.0243	0.0261
Y	0.042	0.039	0.041	0.017	0.011	0.037	0.018	0.024	0.025	0.028	0.023	0.035	0.023	0.051	0.064	0.047	0.050
Total	2.001	1.999	2.001	2.001	1.999	2.008	2.030	2.011	2.019	2.008	2.010	2.007	2.008	2.001	2.004	2.002	2.002
X_{LREE}	0.820	0.818	0.811	0.831	0.894	0.800	0.803	0.856	0.895	0.894	0.842	0.818	0.851	0.835	0.804	0.845	0.862
X_{HREE}	0.045	0.042	0.044	0.021	0.029	0.029	0.026	0.026	0.026	0.027	0.025	0.030	0.027	0.052	0.060	0.049	0.052
X_{hutt}	0.001	0.000	0.001	0.011	0.003	0.008	−0.021	0.010	0.004	0.003	0.012	0.010	0.010	0.014	0.021	0.017	0.009
X_{cher}	0.092	0.101	0.103	0.120	0.063	0.127	0.174	0.085	0.049	0.049	0.098	0.107	0.088	0.047	0.051	0.042	0.027
X_{xno}	0.042	0.039	0.041	0.018	0.012	0.036	0.017	0.023	0.025	0.028	0.023	0.034	0.023	0.051	0.064	0.047	0.050
GH 1997														811	891	782	808
SG 2002														730	805	703	727

Note: GH, monazite–xenotime temperature according to Gratz & Heinrich (1997), SG, according to Seydoux-Guillaume et al. (2002).

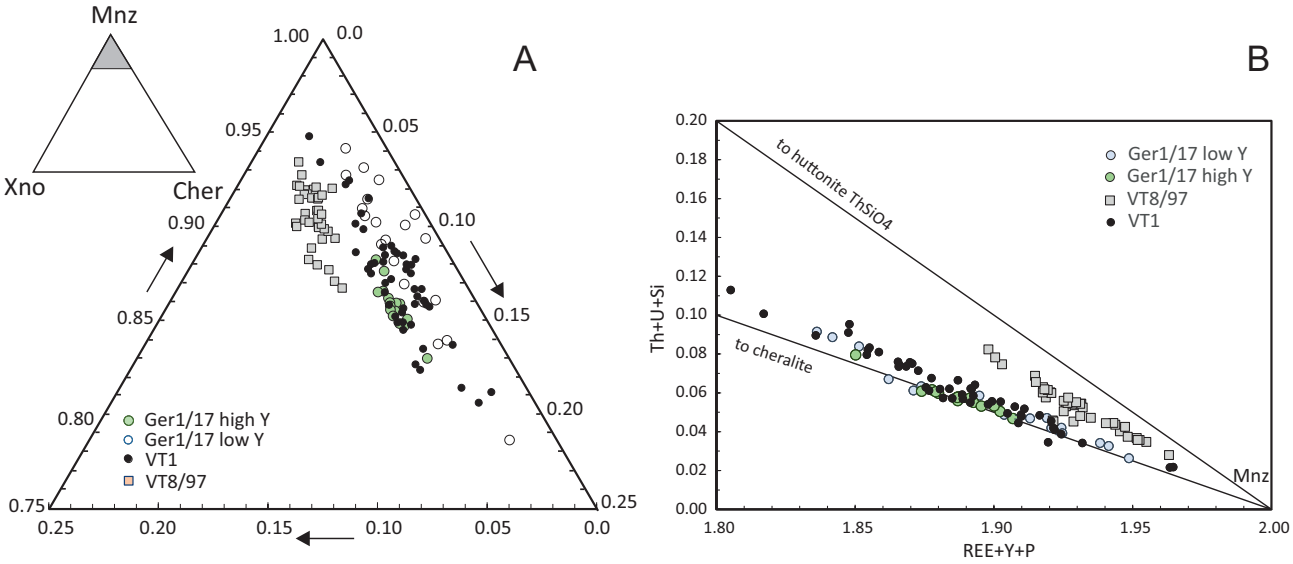

Fig. 16. A — Monazite compositions in the triangle monazite–xenotime–cheralite. **B** — Substitution monazite–cheralite vs. monazite –huttonite.

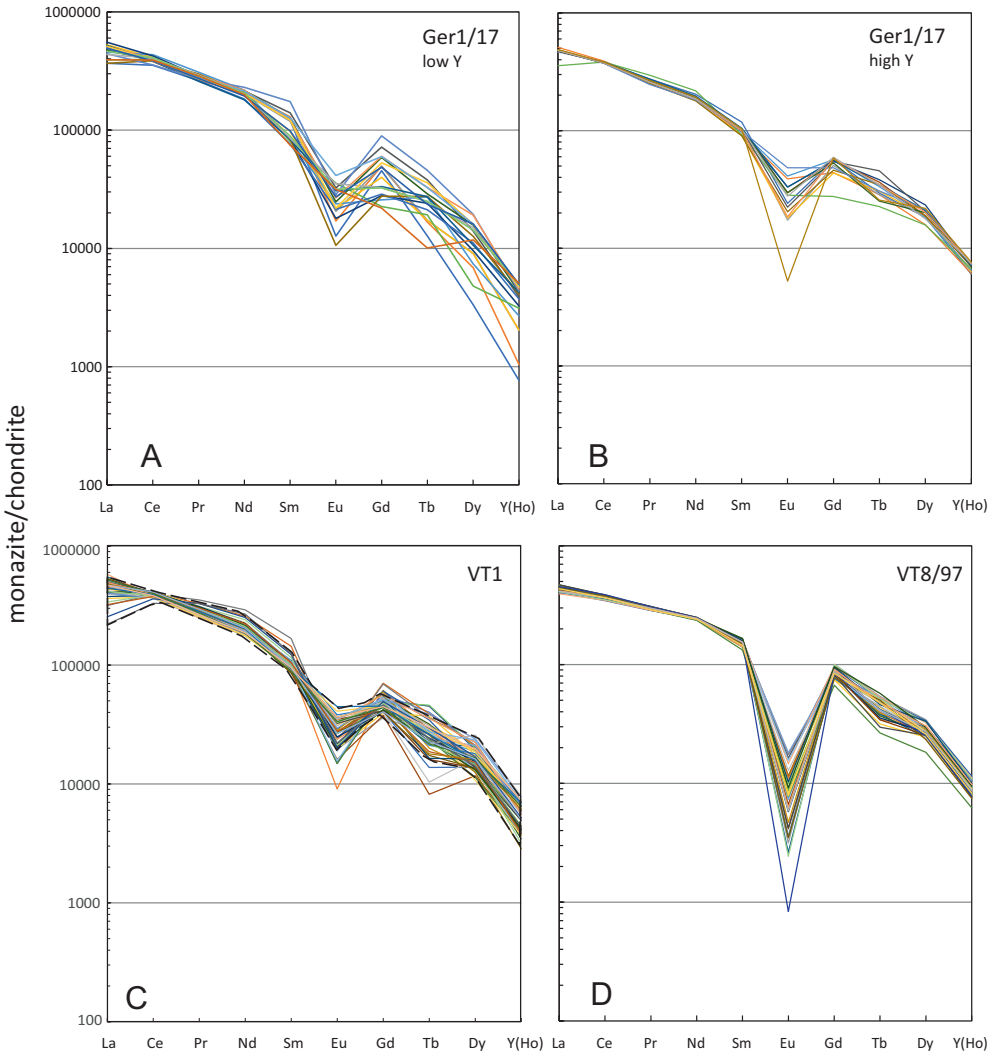

Fig. 17. A–D — The REE distributions patterns in dated monazites from samples Ger1/17, VT1 and VT8/97. Dashed lines refer to the monazite included in garnet.

staurolite persists as rare inclusions in garnets and subhedral crystals in the matrix together with kyanite up to ca. 10 kbar and 600–650 °C (Fig. 12) and it seems to have been eliminated by the reaction

staurolite + muscovite + quartz = garnet + kyanite + biotite + H_2O (R2)

(Janák et al. 1999). However, no persistence of staurolite into the sillimanite zone in the Western Tatra has been observed. The formation of sillimanite in the Western Tatra is interpreted as a result of decomposition reactions of staurolite, kyanite, biotite, garnet and muscovite. In some places, kyanite is partly replaced by sillimanite which is mostly fibrolitic or thin-prismatic, however, most prismatic crystals show no direct transformation from kyanite (Janák et al. 1988, 1999).

In contrast, kyanite is not observed but staurolite is found as inclusions in the garnets of the sillimanite zone metapelites in the High Tatra. This suggests either a total breakdown/replacement of kyanite or a prograde staurolite-to-sillimanite sequence without kyanite development (e.g. Pattison & Spear 2018 and references therein), the latter being our preferred interpretation; a tentative *P–T* path is shown in Fig. 21.

Partial melting

The presence of garnet and K-feldspar in the leucosome of diatexite suggests dehydration melting of biotite and formation of peritectic garnet by the reaction

biotite + sillimanite ± plagioclase + quartz = garnet + K-feldspar + melt (R3)

which has also been suggested in a previous study (Janák et al. 1999). Our new calculations of temperature from oxythermobarometry coupled with biotite TiO_2 isopleths (760–770 °C and 7.5 kbar) in this study (Fig. 13) coincide with biotite fluid-absent melting curve of Le Breton & Thompson (1988) shown in Fig. 21 and are believed to evidence this process. The high TiO_2 biotites (3–3.5 wt%) are probably restitic, surviving the melting event, which consumed other biotites and produced either garnet or Ti-magnetite by reactions (R2, R3) and,

Ti-biotite = ulvöspinel + K-feldspar [$KTiFe_2AlSi_3O_{10}O_2 = Fe_2TiO_4 + KAlSi_3O_8$] (R4)

Plagioclase (An_{25}) was involved in the melt as suggested by the location of $An_{25–29}$ isopleths just above solidus. Crossing the muscovite-in curve mostly in subsolidus conditions caused the replacement of sillimanite (fibrolite) by muscovite. Pure magnetite with voids probably originally containing fluid is explained as a product of biotite (annite) oxidation by the reaction

annite + $1/2O_2$ = magnetite + K-feldspar + H_2O (R5)

The preserved high-annite biotite would provide enough Fe to produce the magnetite. An analogous process of late oxidation was identified in I-type tonalites from the Tribeč Mts.

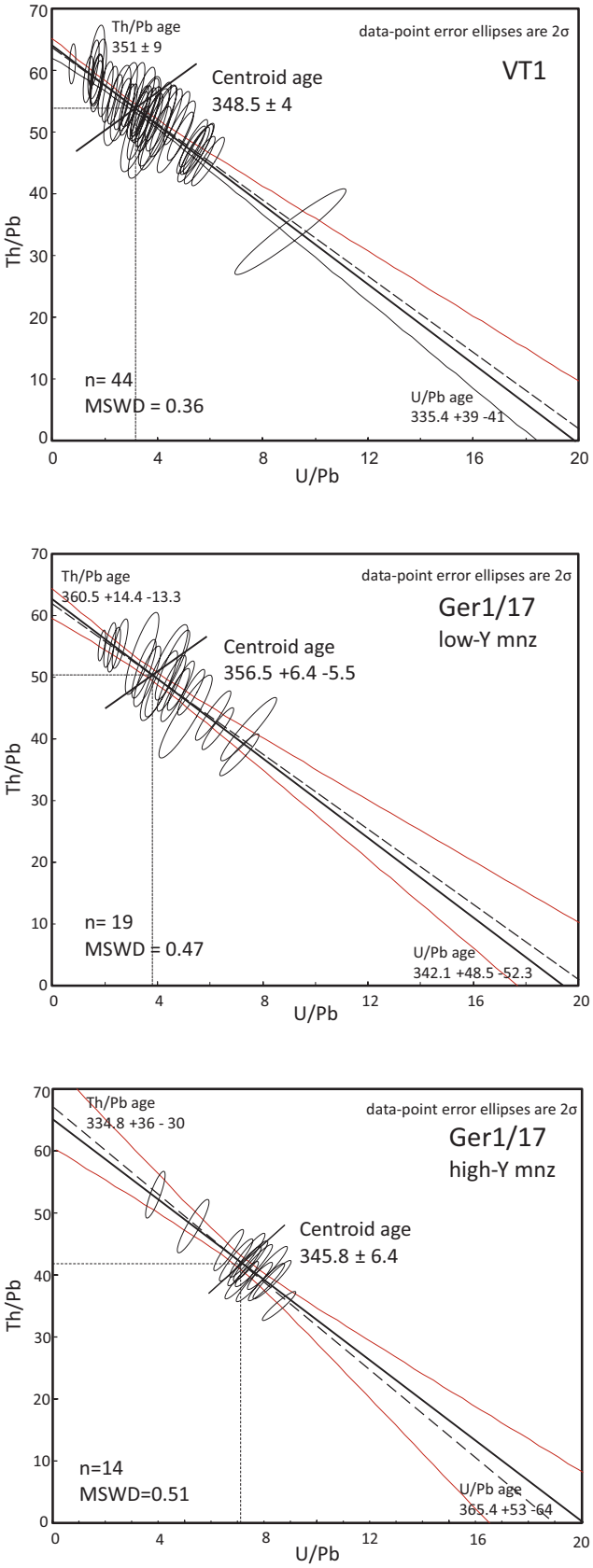

Fig. 18. U/Pb vs Th/Pb isochrons (Cocherie & Albarede 2001) of the dated samples VT1 and Ger1/17.

(Broska & Petrík 2011, 2015) and has been suggested earlier for I-type granite suites (Czamanske et al. 1981).

Thermodynamic modelling of leucosome indicates ca. 80–85 vol% of the melt for the inferred peak conditions, 700–760 °C (Fig. 13). This sample not only has monazite with the highest Y contents but also contains xenotime, which suggests that Y was close to saturation and its Y contents may be used to calculate temperature (Heinrich et al. 1997; Gratz & Heinrich 1997; Seydoux-Guillaume et al. 2002). The obtained temperatures from monazite-xenotime thermometry vary according to various calibrations, the empirical thermometer by Gratz & Heinrich (1997) yields the highest values 750–900 °C. The calibration according to Seydoux-Guillaume et al. (2002) gives a lower range of 650–800 °C, mostly in hypersolidus region. This calibration corrects temperatures according to $ThSiO_4$ component in monazite at X_{ThSiO4}=0.09. The VT8/97 monazite has a lower X_{ThSiO4}=0.005–0.02 requiring less correction, which implies that the calculated temperatures would represent a lower estimate. The monazite–xenotime thermometer thus supports magmatic origin of the monazite.

Table 7: Results of monazite el. microprobe dating.

Sample	Age	2σ	MSWD	n	Method
Ger1/17 low Y	356.5	6.4	0.47	19	isochron
Ger1/17 high Y	345.8	6.4	0.51	14	isochron
VT1	348.5	4	0.36	63	isochron
VT8/97	351.5	5.1	0.36	32	wa
T8	349.7	3.7	1.3	62	wa

Note: wa, weighted average

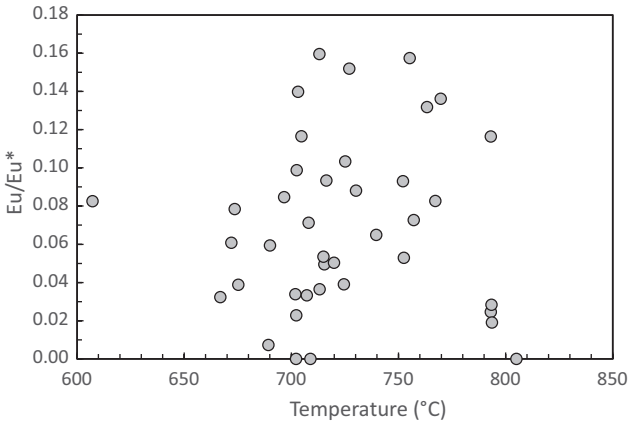

Fig. 19. Correlation of temperature (monazite–xenotime thermometer, Seydoux-Guillaume et al. 2002) with Eu anomalies in the sample VT8/97.

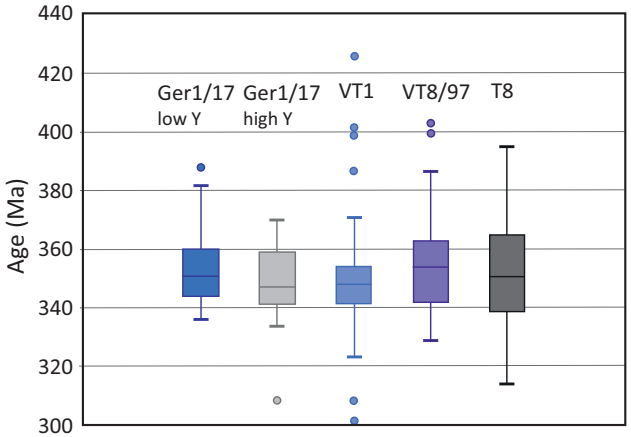

Fig. 20. Comparison of all monazite samples in a box-and-whiskers plot. Horizontal bars refer to averages, all data are shown including outliers not used in the age calculations.

The REE patterns in VT8/97 monazite show large negative Eu anomalies, which correlate positively with Y contents. Taking Y as a proxy for temperature, the positive correlation indicates increasing negative Eu anomaly with decreasing temperature (Fig. 19). As the redox regime does not change significantly in hypersolidus region (the melt at 700–770 °C is reduced with O_2 content in the system 0.005 wt%), the plagioclase crystallization may have been responsible for the decreasing Eu. Indeed, according to the pseudosection model (Fig. 13), the amount of plagioclase increases from 5 vol% at 770 °C to 18 vol% near solidus, which explains deepening of the negative Eu anomalies.

Monazite composition and age data

The dated monazites according to their compositions split into two groups, metamorphic and those crystallized from the melt (Fig. 20). The first group is relatively homogeneous showing no significant difference between monazites from matrix and relatively rare monazites included in garnet. The second group not only has the highest Y and large negative Eu anomalies but differs also in being distinctly shifted to monazite–huttonite substitution trend. The first two features are attributed to their magmatic origin, highest temperature and feldspar crystallization, the last probably due to much higher SiO_2 of the VT8/97 whole rock.

The obtained ages are identical within 2σ errors and indicate that both metamorphic and melting events occurred between 350–345 Ma. The distinction of 5 Ma is beyond the ability of the monazite chemical dating method, nevertheless, the older age of 351±5 Ma for leucosome VT8/97 is in accordance with its higher *P–T* conditions: magmatic monazite may date an earlier Th–U–Pb system closure at higher temperature than monazites from metapelites VT1 and high-Y monazite Ger1/17 (around 345 Ma). The individual points from the low-Y monazite (356.5±6 Ma) may have partly targeted some inherited domains or older metamorphic monazites. It is noted that in the Western Tatra isotopic monazite dating revealed an older eo-Variscan event at ca. 380 Ma (Moussalam et al. 2012) as discussed below.

Tectonic implications

SIMS U–Pb zircon age data from the retrogressed eclogite in the Western Tatra (Baranec) by Burda et al. (2021) recorded two zircon forming events: (1) 367 Ma, interpreted as a mini-

mum age for eclogite facies metamorphism, and (2) 349 Ma, interpreted as retrogression under amphibolite facies conditions (see Fig. 21). ID-TIMS Sm–Nd garnet dating of eclogite from the same locality and sample studied previously by Janák et al. (1996) yields a whole rock-garnet "clean" isochron age of 342±11 Ma interpreted as post-eclogite garnet re-equilibration (Moussallam et al. 2012). In situ U–Pb dating by LA-ICPMS method of monazite from a migmatitic paragneiss in the kyanite zone, adjacent to the eclogite, shows one age population of ca. 380 Ma whereas a migmatite in a distance of ca. 5km SE from the eclogite records 340±11 Ma age (Moussallam et al. 2012). SIMS U–Pb dating of zircons in the leucosome of the sillimanite zone migmatite in the Western Tatra dated by Moussallam et al. (2012) yielded 347±7 Ma age. These data suggest that subduction and high-pressure, eclogite facies metamorphism (M1) at P>15 kbar/700 °C occurred in Late Devonian. Both retrogressed eclogite and kyanite-bearing gneiss show equillibration under high-pressure granulite/high-pressure amphibolite facies conditions (ca. 10–14 kbar/700–750 °C, Janák et al. 1996, 1999). Early Carboniferous medium-pressure/high-temperature metamorphism (M2) between ca. 350–340 Ma is also recorded by our dating of monazite in sillimanite-bearing gneisses and migmatites (Fig. 21), and interpreted as a consequence of crustal thickening. Considering the age data there was the age gap at least 20 Myr between HP metamorphism (M1) and MP/HT metamorphism (M2). Decompression of high-grade, partially melted migmatites overlapped intrusion and emplacement of the granitoid pluton at ca. 350–340 Ma according to geochronological data from zircon in granitoids (Poller et al. 2001; Burda et al. 2013; Gawęda et al. 2016, 2018; Kohút & Larionov 2021; Broska et al. 2022). Recently published SHRIMP U–Pb zircon ages of 359.2±3 Ma in diorite enclave and 350.1±2.6 Ma in host granodiorite intrusion from the High Tatra (Broska et al. 2022) are interpreted as a timing of granitoid magmatism related to break-off of subucted slab, which may allow heating from asthenospheric material replacing the subducting slab. This input of heat may drive melting leading to granitoid magmatism, which may in turn facilitate detachment and exhumation (e.g. Warren 2013). The age of 350 Ma is supported also by our monazite dating of granodiorite. The coeval granitic magmatism is, however, not considered as the cause of the dated metamorphism which is of regional extent and a consequence of crustal thickening. Uplift and cooling took place between ca. 340–300 Ma, as recorded by Ar–Ar dating of biotite in metapelitic gneiss in the High Tatra (Janák & Onstott 1993; Janák 1994) and U–Pb zircon, titanite and apatite dating of metamorphic rocks in the Western Tatra (Gawęda et al. 2018). Exhumation and inversion of the metamorphic sequence occurred in a contractional setting by top-to-the-south, southeast thrusting and emplacement of the upper unit onto the lower one. Overall, there are similarities, such as – metamorphic inversion, where a high-grade unit comprising migmatites with relicts of eclogite has been thrust over a lower-grade mica schist, intrusion of granite accommodated in the hangingwall and coeval with high-grade metamorphism,

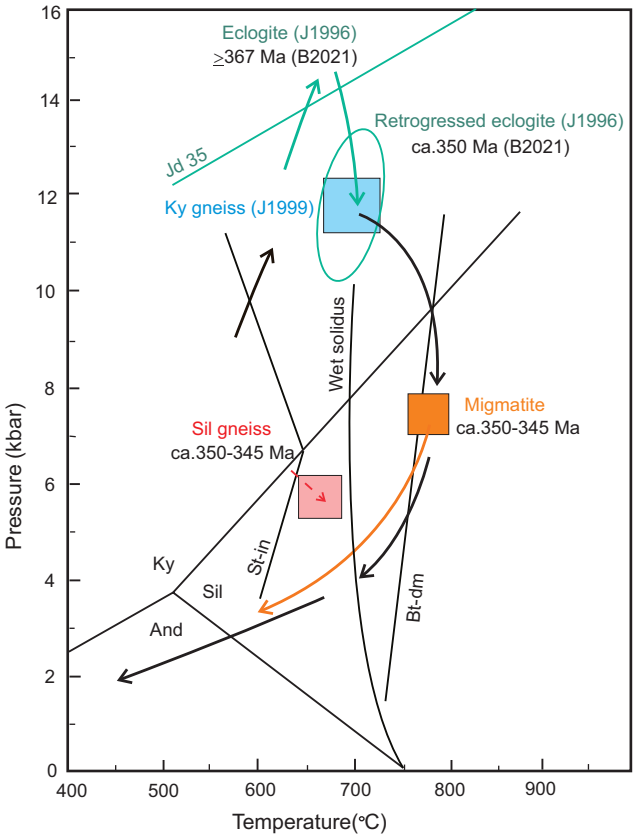

Fig. 21. Metamorphic conditions and *P–T* paths of the Tatra Mts. upper unit lithologies. Peak metamorphic conditions (pink box) and *P–T* path (red dashed arrow) of sillimanite gneiss Ger1/17 (red box) and migmatite VT8/97 (brown box and arrow) with monazite ages from this study. Metamorphic conditions and *P–T* path of retrogressed eclogites (green ellipsoid, green arrow) from Janák et al. (1996), and eclogite zircon ages from Burda et al. (2021). Metamorphic conditions of kyanite gneiss (blue box) associated with retrogressed eclogite and *P–T* path of the upper unit metapelites (black arrow) according to Janák et al. (1999). Dehydration–melting curve of biotite according to Le Breton & Thompson (1988).

with tectono-metamorphic records of collisional Himalaya-Tibet orogen (e.g. Kohn 2014; Weller et al. 2021 and references therein). However, mechanisms of metamorphic inversion in the Tatra Mts. are less understood and need to be critically tested.

Conclusions

The results from thermodynamic modelling and age data on monazite from high-grade metapelites of the High Tatra Mountains constrain metamorphism and partial melting in the Early Carboniferous, at ca. 350–345 Ma, as a consequence of continental collision and crustal thickening in the course of Variscan orogeny.

Monazite compositions from metapelitic gneisses differ from those from leucosome part of migmatite. The latter show pronounced Eu-negative anomalies interpreted as the result of

co-crystallization with feldspars and higher Y contents indicating higher temperature of crystallization. In metapelitic gneisses, the contents of Y enclosed in garnet do not differ from those occurring in the matrix.

The metapelitic gneisses followed a prograde *P–T* path via staurolite-to-sillimanite sequence reactions attaining peak metamorphic conditions ca. 5–6 kbar and 650–700 °C, at mid-crustal levels.

Migmatites underwent partial melting involving biotite dehydration reactions and formation of peritectic garnet in the leucosome at ca. 7–8 kbar and 760–770 °C, during decompression from lower-crustal levels.

Acknowledgements: We thank J. Majka and J. Kotková for their constructive reviews. F. Finger is thanked for XRF analysis of the sample VT8/97, S. Milovská and V. Sasinková for Raman analysis. This work was supported by the Slovak Research and Development Agency under grant project APVV-18-0107, and Scientific grant agency VEGA (projects 2/0056/20, 2/0008/19).

References

Anderson A.T. & Lindsley D.H. 1985: New (and final!) model for the Ti-magnetite/ilmenite geothermometers and oxygen barometers. *Transaction American Geophysical Union* 66, 416.

Andrusov D. 1968: Grundriss der Tektonik der Nordlichen Karpathen. *Veda Publishing House, Bratislava*.

Broska I. & Petrík I. 2011: Accessory Fe–Ti oxides in the West Carpathian I-type granitoids: witnesses of the granite mixing and late oxidation processes. *Mineralogy and Petrology* 101, 87–97. https://doi.org/10.1007/s00710-011-0158-6

Broska I. & Petrík I. 2015: Variscan thrusting in I- and S-type granitic rocks of the Tribeč Mountains, Western Carpathians (Slovakia): evidence from mineral compositions and monazite dating. *Geologica Carpathica* 66, 455–471. https://doi.org/10.1515/geoca-2015-0038

Broska I., Janák M., Svojtka M., Yi K., Konečný P., Kubiš M., Kurylo S., Hrdlička M. & Maraszewska M. 2022: Variscan granitic magmatism in the Western Carpathians with linkage to slab break-off. *Lithos* 412–413. https://doi.org/10.1016/j.lithos.2021.106589

Bukała M., Barnes C.J., Jeanneret P., Hidas K., Mazur S., Almqvist B.S.G., Kosminska K., Klonowska I., Šurka J. & Majka J. 2020: Brittle deformation during eclogitization of Early Paleozoic Blueschist. *Frontiers in Earth Science* 8, 594453. https://doi.org/10.3389/feart.2020.594453

Burda J., Gawęda A. & Klötzli U. 2013a: Geochronology and petrogenesis of granitoid rocks from the Goryczkowa Unit, Tatra Mountains (Central Western Carpathians). *Geologica Carpathica* 64, 419–435. https://doi.org/10.2478/geoca-2013-0029

Burda J., Gawęda A. & Klötzli U. 2013b: U–Pb zircon age of the youngest magmatic activity in the High Tatra granites (Central Western Carpathians). *Geochronometria* 40, 134–144. https://doi.org/10.2478/s13386-013-0106-9

Burda J., Klötzli U., Majka J., Chew D., Li Q-L., Liu Y., Gawęda A. & Wiedenbeck M. 2021: Tracing proto-Rheic – Qaidam Ocean vestiges into the Western Tatra Mountains and implications for the Palaeozoic palaeogeography of Central Europe. *Gondwana Research* 91, 188–204. https://doi.org/10.1016/j.gr.2020.12.016

Caddick M.J., Konopásek J. & Thompson A.B. 2010: Preservation of garnet growth zoning and the duration of prograde metamorphism. *Journal of Petrology* 51, 2327–2347. https://doi.org/10.1093/petrology/egq059

Carlson W.D. 2006: Rates of Fe, Mg, Mn and Ca diffusion in garnet. *American Mineralogist* 91, 1–11. https://doi.org/10.2138/am.2006.2043

Catlos E., Gilley L.D. & Harrison T.M. 2002: Interpretation of monazite ages obtained via in situ analysis. *Chemical Geology* 188, 193–215. https://doi.org/10.1016/S0009-2541(02)00099-2

Clemens J.D. & Vielzeuf D. 1987: Constraints on melting and magma production in the crust. *Earth and Planetary Sciences Letters* 86, 287–306. https://doi.org/10.1016/0012-821X(87)90227-5

Cocherie A. & Albarede F. 2001: An improved U–Th–Pb age calculation for electron microprobe dating of monazite. *Geochimica et Cosmochimica Acta* 65, 4509–4522. https://doi.org/10.1016/S0016-7037(01)00753-0

Connolly J.A.D. 2005: Computation of phase-equilibria by linear programming: A tool for geodynamic modeling and its application to subduction zone decarbonation. *Earth and Planetary Science Letters* 236, 524–541. https://doi.org/10.1016/j.epsl.2005.04.033

Czamanske G.K., Ishihara Sh. & Atkin S.A. 1981: Chemistry of rock-forming minerals of the Cretaceous-Paleocene batholith in southwestern Japan and implications for magma genesis. *Journal of Geophysical Research* 86, 10431–10469. https://doi.org/10.1029/JB086iB11p10431

Engi M. 2017: Petrochronology based on REE-minerals: Monazite, allanite, xenotime, apatite. In: Kohn M.J., Engi M. &. Lanari P. (Eds.): Petrochonology: Methods and applications. https://doi.org/10.1515/9783110561890-013

Finger F., Broska I., Roberts M.P. & Schermeier A. 1998: Replacement of primary monazite by apatite-allanite-epidote coronas in an amphibolite facies granite gneiss from the eastern Alps. *American Mineralogist* 83, 248–258. https://doi.org/10.2138/am-1998-3-408

Finger F., Broska I., Haunschmied B., Hraško L., Kohút M., Krenn E., Petrík I., Riegler G. & Uher. P. 2003: Electron-microprobe dating of monazites from Western Carpathian basement granitoids: plutonic evidence for an important Permian rifting event subsequent to Variscan crustal anatexis. *International Journal of Earth Sciences* 92, 86–98. https://doi.org/10.1007/s00531-002-0300-0

Fritz H., Neubauer F., Janák M. & Putiš M. 1992: Variscan mid-crustal thrusting in the Carpathians II: Kinematics and fabric evolution of the Western Tatra basement. *Terra Abstracts*, Supplement 2 to *Terra Nova* 4, 24.

Fuhrman M.L. & Lindsley D.H. 1988: Ternary-feldspar modeling and thermometry. *American Mineralogist* 73, 201–215.

Gawęda A., Burda J., Klötzli U., Golonka J., Szopa K. 2016: Episodic construction of the Tatra granitoid intrusion (Central Western Carpathians, Poland/Slovakia): consequences for the geodynamics of Variscan collision and Rheic Ocean closure. *International Journal of Earth Sciences (Geologische Rundschau)* 105, 1153–1174. https://doi.org/10.1007/s00531-015-1239-2

Gawęda A., Szopa K., Chew D., O'Sullivan G.J., Burda J., Klötzli U. & Golonka J. 2018: Variscan post-collisional cooling and uplift of the Tatra Mountains crystalline block constrained by integrated zircon, apatite and titanite LA-(MC)-ICP-MS U-Pb dating and rare earth element analyses. *Chemical Geology* 484, 191–209. https://doi.org/10.1016/j.chemgeo.2018.03.012

Ghiorso M.S. & Evans B.W. 2008: Thermodynamics of rhombohedral oxide solid solutions and a revision of the Fe-Ti two oxide geothermometer and oxygen-barometer. *American Journal of Science* 308, 957–1039. https://doi.org/10.2475/09.2008.01

Gieré R., Rumble D., Günther D., Connolly J. & Caddick M.J. 2011: Correlation of growth and breakdown of major and accessory minerals in metapelites from Campolungo, Central Alps. *Journal of Petrology* 52, 2293–2334. https://doi.org/10.1093/petrology/egr043

Giuntoli F., Lanari P. & Engi M. 2018: Deeply subducted continental fragments – Part 1: fracturing, dissolution–precipitation, and diffusion processes recorded by garnet textures of the central Sesia Zone (western Italian Alps). *Solid Earth* 9, 167–189. https://doi.org/10.5194/se-9-167-2018

Gorek A. 1959: An outline of geological and petrographical relationships in the Crystalline complexes of the Tatra Mts. *Geologický Zborník SAV* 10, 13–88.

Gratz R. & Heinrich W. 1997: Monazite-xenotime themrobarometry: experimental calibration of the miscibility gap in the binary system $CePO_4$–YPO_4. *American Mineralogist* 82, 772–780. https://doi.org/10.2138/am-1997-7-816

Hacker B., Kylander-Clark A. & Holder R. 2019: REE partitioning between monazite and garnet: Implications for petrochronology. *Journal of Metamorphic Geology* 37, 227–237. https://doi.org/10.1111/jmg.12458

Heinrich W., Andrehs G. & Franz G. 1997: Monazite–xenotime miscibility gap thermometry. I. An empirical calibration. *Journal of Metamorphic Geology* 15, 3–16. https://doi.org/10.1111/j.1525-1314.1997.t01-1-00052.x

Hermann J. & Rubatto D. 2003: Relating zircon and monazite domains to garnet growth zones: age and duration of granulite facies metamorphism in the Val Malenco lower crust. *Journal of Metamorphic Geology* 21, 833–852. https://doi.org/10.1046/j.1525-1314.2003.00484.x

Holland T.J.B. & Powell R. 2011: An improved and extended internally consistent thermodynamic dataset for phases of petrological interest, involving a new equation of state for solids. *Journal of Metamorphic Geology* 29, 333–383. https://doi.org/10.1111/j.1525-1314.2010.00923.x

Janák M. 1993: Calc-silicate metamorphic rocks of the High Tatra crystalline basement. *Mineralia Slovaca* 25, 177–182.

Janák M. 1994: Variscan uplift of the crystalline basent, Tatra Mts., Central Western Carpathians: evidence from $^{40}Ar/^{39}Ar$ laser probe dating of biotite and P–T–t paths. *Geologica Carpathica* 45, 293–300.

Janák M. & Onstott T.C. 1993: Pre-Alpine tectono-thermal evolution of metamorphism in the Tatra Mts., Western Carpathians: P–T paths and $^{40}Ar/^{39}Ar$ laser probe dating. *Terra Abstracts* supplement 1 to *Terra Nova* 5, 238.

Janák M., Kahan Š. & Jančula D. 1988: Metamorphism of pelitic rocks and metamorphic zones in SW part of Western Tatra Mts. Crystalline complexes. *Geologický Zborník – Geologica Carpathica* 39, 455–488.

Janák M., O´Brien P.J., Hurai V. & Reutel C. 1996: Metamorphic evolution and fluid composition of garnet-clinopyroxene amphibolites from the Tatra Mountains, Western Carpathians. *Lithos* 39, 57–79. https://doi.org/10.1016/S0024-4937(96)00019-9

Janák M., Hurai V., Ludhová L. O´Brien P.J. & Horn E.E.1999: Dehydration melting and devolatilization of high-grade metapelites: the Tatra Mountains, Western Carpathians. *Journal of Metamorphic Geology* 17, 379–396. https://doi.org/10.1046/j.1525-1314.1999.00206.x

Janots E., Engi M., Berger A., Allaz J., Schwarz J.-O. & Spandler C. 2008: Prograde metamorphic sequence of REE minerals in pelitic rocks of the central Alps: implications for allanite–monazite–xenotime phase relations from 250 to 610 °C. *Journal of Metamorphic Geology* 26, 509–526. https://doi.org/10.1111/j.1525-1314.2008.00774.x

Kahan Š. 1969: Eine neue Ansicht über den geologischen Aufbau des Kristallinikums der West Tatra. *Acta Geologica et Geographica Universitatis Comenianae* 12, 115–122.

Kohn M.J. 2014: Himalayan metamorphism and its tectonic implications. *Annual Review of Earth and Planetary Sciences* 42, 381–419. https://doi.org/10.1146/annurev-earth-060313-055005

Kohn M.J. & Spear F. 2000: Retrograde net transfer reaction insurance for pressure-temperature estimates. *Geology* 28, 1127–1130. https://doi.org/10.1130/0091-7613(2000)028%3C1127:RNTRIF%3E2.3.CO;2

Kohn M.J., Wieland M.S., Parkinson C.D. & Upreti B.N. 2005: Five generations of monazite in Langtang gneisses: implications for chronology of Himalayan metamorphic core. *Journal of Metamorphic Geology* 23, 399–406. https://doi.org/10.1111/j.1525-1314.2005.00584.x

Kohút M. & Janák M. 1994: Granitoids of the Tatra Mts., Western Carpathians: field relationships and petrogenetic implications. *Geologica Carpathica* 45, 301–311.

Kohút M. & Larionov A.N. 2021: From subduction to collision: Genesis of the Variscan granitic rocks from the Tatric Superunit (Western Carpathians, Slovakia). *Geologica Carpathica* 72, 96–113. https://doi.org/10.31577/GeolCarp.72.2.2

Konečný P., Kusiak M.A. & Dunkley D.J. 2018: Improving U–Th–Pb electron microprobe dating using monazite age references. *Chemical Geology* 484, 22–35. https://doi.org/10.1016/j.chemgeo.2018.02.014

Konrad-Schmolke M., O'Brien P.J. & Heidelbach F. 2007: Compositional reequilibration of garnet: the importance of sub-grain boundaries. *European Journal of Mineralogy* 19, 431–438. https://doi.org/10.1127/0935-1221/2007/0019-1749

Krenn E., Janák M., Finger F., Broska I. & Konečný P. 2009: Two types of metamorphic monazite with contrasting La/Nd, Th, and Y signatures in an ultrahigh-pressure metapelite from the Pohorje Mountains, Slovenia: Indications for pressure-dependent REE exchange between apatite and monazite? *American Mineralogy* 89, 1323–1329. https://doi.org/10.2138/am.2009.2981

Le Breton N. & Thompson A.B. 1988: Fluid-absent (dehydration) melting melting of biotite in metapelites in the early stages of crustal anatexis. *Contributions to Mineralogy and Petrology* 99, 226–237. https://doi.org/10.1007/BF00371463

Ludwig K.R. 2001: User manual for Isoplot/Ex ver. 2.49. A geochronological toolkit for Microsoft Excel. *Berkeley Geochronological Centre Special Publications* 1a, 1–56.

Majka J., Be'eri-Shlevin Y., Gee D.G., Ladenberger A., Claesson S., Konečný P. & Klonowska I. 2012: Multiple monazite growth in the Åreskutan migmatites: evidence for a polymetamorphic Late Ordovician to Late Silurian evolution in the Seve Nappe Complex of the west-central Jämtland, Sweden. *Journal of Geosciences* 57, 3–23. https://doi.org/10.3190/jgeosci.112

Montel J.-M., Foret S., Veschambre M., Nicollet Ch. & Provost A. 1996: Electron microprobe dating of monazite. *Chemical Geology* 131, 37–53. https://doi.org/10.1016/0009-2541(96)00024-1

Moussallam Y., Schneider D.A., Janák M., Thöni M. & Holm D.K. 2012: Heterogeneous extrusion and exhumation of deep-crustal Variscan assembly: Geochronology of the Western Tatra Mountains, northern Slovakia. *Lithos* 144, 88–108. https://doi.org/10.1016/j.lithos.2012.03.025

Parrish R.R. 1990: U–Pb dating of monazite and its application geological problems. *Canadian Journal of Earth Sciences* 27, 1431–1450. https://doi.org/10.1139/e90-152

Pattison D.R.M. & Spear F.S. 2018: Kinetic control of staurolite-Al_2SiO_5 mineral assemblages: Implications for Barrovian and Buchan metamorphism. *Journal of Metamorphic Geology* 36, 667–690. https://doi.org/10.1111/jmg.12302

Pawlica W. 1918: Garluchowskie skaly wapieno-krzemianowe [Calc-silicate rocks from Gerlach]. *Rozprawy Wydziału Matematyczno-Przyrodniczego Akademii Umiejętności* 13,107–130 (in Polish).

Petrík I. & Konečný P. 2009: Metasomatic replacement of inherited metamorphic monazite in a biotite-garnet granite from the Nízke Tatry Mountains, Western Carpathians, Slovakia: Chemical dating and evidence for disequilibrium melting. *American Mineralogist* 94, 957–974. https://doi.org/10.2138/am.2009.2992

Petrík I., Janák M., Klonowska I., Majka J., Froitzheim N., Yoshida K., Sasinková V., Konečný P. & Vaculovič T. 2019: Monazite behaviour during metamorphic evolution of a diamond-bearing gneiss: a case study from the Seve Nappe Complex, Scandinavian Caledonides. *Journal of Petrology* 60, 1773–1796. https://doi.org/10.1093/petrology/egz051

Petrík I., Janák M., Vaculovič T., Konečný P., Méres Š. 2020: Variscan high-pressure metamorphism of kyanite-bearing paragneisses hosting eclogites in the Veporic unit, Western Carpathians: Evidence from Th–U–Pb dating of monazite. *Geologica Carpathica* 71, 485–502. https://doi.org/10.31577/GeolCarp.71.6.1

Plašienka D., Grecula P., Putiš M., Hovorka D. & Kováč M. 1998: Evolution and structure of the Western Carpathians: an overview. In: Grecula P., Hovorka D. & Putiš M. (Eds.): Geological Evolution of the Western Carpathians. *Mineralia Slovaca – Monograph*, 1–24.

Plašienka D. 2018: Continuity and episodicity in the Early Alpine tectonic evolution of the Western Carpathians: how large-scale processes are expressed by the orogenic architecture and rock record data. *Tectonics* 37, 2029–2079. https://doi.org/10.1029/2017TC004779

Poller U. & Todt W. 2000: U–Pb single zircon data of granitoids from the High Tatra Mountains (Slovakia): implications for the geodynamic evolution. *Transactions of the Royal Society of Edinburgh Earth Sciences* 91, 235–243. https://doi.org/10.1017/S0263593300007409

Poller U., Janák M., Kohút M. & Todt W. 2000: Early Variscan magmatism in the Western Carpathians: U–Pb zircon data from granitoids and orthogneisses of the Tatra Mountains (Slovakia). *International Journal of Earth Sciences* 89, 336–349. https://doi.org/10.1007/s005310000082

Poller U., Huth J., Hoppe P. & Williams I.S. 2001: REE, U, Th, and Hf distribution in zircon from Western Carpathian Variscan granitoids: a combined cathodoluminescence and ion microprobe study. *American Journal of Science* 301, 858–867. https://doi.org/10.2475/ajs.301.10.858

Pyle J.M., Spear F.S., Rudnick R.L. & McDonough W.F. 2001: Monazite–xenotime–garnet equilibrium in metapelites and a new monazite-garnet thermometer. *Journal of Petrology* 42, 2083–2107. https://doi.org/10.1093/petrology/42.11.2083

Seydoux-Guillaume A-M., Wirth R., Heinrich W. & Montel J.-M. 2002: Experimental determination of Thorium partitioning between monazite and xenotime using electron microscopy and X-ray diffraction Rietveld analysis. *European Journal of mineralogy* 14, 869–878. https://doi.org/10.1127/0935-1221/2002/0014-0869

Skrzypek E., Bosse V., Kawakami T., Martelat J-E. & Štípská P. 2017: Transient allanite replacement and prograde to retrograde monazite (re)crystallization in medium-grade metasedimentary rocks from the Orlica-Śnieżnik Dome (Czech Republic/Poland): Textural and geochronological arguments. *Chemical Geology* 449, 41–57. https://doi.org/10.1016/j.chemgeo.2016.11.033

Spear F.S. 1991: On the interpretation of peak metamorphic temperatures in light of garnet diffusion during cooling. *Journal of Metamorphic Geology* 9, 379–388. https://doi.org/10.1111/j.1525-1314.1991.tb00533.x

Spear F.S. & Pyle J.M. 2002: Apatite, monazite and xenotime in metamorphic rocks. *Reviews in Mineralogy* 48, 293–335. https://doi.org/10.1515/9781501509636-010

Suzuki K. & Adachi M. 1991: The chemical Th–U-total Pb isochron ages of zircon and monazite from the Grey granite of the Hida terrane, Japan. *The Journal of Earth Sciences, Nagoya University* 38, 11–38.

Suzuki K. & Kato T. 2008: CHIME dating of monazite, xenotime, zircon and polycrase: Protocol, pitfall and chemical criterion of possibly discordant age data. *Gondwana Research* 14, 569–586. https://doi.org/10.1016/j.gr.2008.01.005

Terry M.P., Robinson P., Hamilton M.A. & Jercinovic M. J. 2000: Monazite geochronology of UHP and HP metamorphism, deformation, and exhumation, Nordoyane, Western Gneiss Region, Norway. *American Mineralogist* 85, 1651–1664. https://doi.org/10.2138/am-2000-11-1208

Warren C.J. 2013: Exhumation of (ultra-)high-pressure terranes: concepts and mechanisms. *Solid Earth* 4, 75–92. https://doi.org/10.5194/se-4-75-2013

Weller O.M., Mottram C.M., St-Onge M.R., Möller Ch., Strachan R., Rivers T. & Copley A. 2021: The metamorphic and magmatic record of collisional orogen. *Nature Reviews Earth & Environment* 2, 781–799. https://doi.org/10.1038/s43017-021-00218-z

White R.W., Powell R., Holland T.J.B., Johnson T.E. & Green E.C.R. 2014: New mineral activity–composition relations for thermodynamic calculations in metapelitic systems. *Journal of Metamorphic Geology* 32, 261–286. https://doi.org/10.1111/jmg.12071

Whitney D.L. & Evans B.W. 2010: Abbreviations for names of rock-forming minerals. *American Mineralogist* 95, 185–187. https://doi.org/10.2138/am.2010.3371

Zhu X. K. & O'Nions R. K. 1999: Monazite chemical composition: some implications for monazite geochronology. *Contributions to Mineralogy and Petrology* 137, 351–363. https://doi.org/10.1007/s004100050555

Electronic supplementary Table S1 is available online at http://geologicacarpathica.com/data/files/supplements/GC-73-2-Janak_Suppl_Table_S1.xlsx